Mechanical Systems and Signal Processing 121 (2019) 856–875

Contents lists available at ScienceDirect

Mechanical Systems and Signal Processing

journal homepage: www.elsevier.com/locate/ymssp

# A new way for harmonic probing of hysteretic systems through nonlinear smooth operators

Rafael de O. Teloli *, Samuel da Silva

*UNESP – Universidade Estadual Paulista, Faculdade de Engenharia de Ilha Solteira, Departamento de Engenharia Mecânica, Av. Brasil, 56, Ilha Solteira, 15385-000 SP, Brasil*

ARTICLE INFO

*Article history:*
Received 28 September 2018
Received in revised form 12 November 2018
Accepted 26 November 2018
Available online 13 December 2018

*Keywords:*
Hysteretic systems
Higher-order frequency response function
Harmonic probing
Volterra series

ABSTRACT

This paper proposes a new way to approach hysteresis with the rate-independent property through an analytical response for the non-smooth hysteresis loop using frequency response approximations. The method consists of rewriting the loading and unloading loop using smooth operators and after applying a harmonic probing in the equivalent system to obtain the higher-order frequency response functions computed by Volterra series. The novelty of this paper lies on predicting analytically, through closed-form equations of the Volterra kernels, the output and the hysteresis loop from a non-smooth system. To illustrate the applicability of the proposed approach, a challenging benchmark with hysteretic damping, described by the Bouc-Wen model, is simulated through a numerical integration scheme. The hysteresis loops, as well as the outputs, are compared to the analytical approach proposed here. The results show that the Volterra model is able to predict the hysteretic outputs when the excitation amplitude is weak and the hysteresis draws a single loop in the restoring force × displacement plane. The higher-order FRFs are given as a function of the model parameters. This framework could turn into an alternative tool to perform nonlinear modal analysis on a hysteretic system.



## 1. Introduction

The hysteresis effect is a nonlinear phenomenon described by a lag between the input and output involving memory mechanisms [1]. They are found in many applications, for instance, energy dissipation and vibration isolators [2–5], bolted joints in assembled structures [6], friction dynamics [7,8], etc. The models commonly used to describe the complexity of real hysteretic systems are mostly phenomenological and seek to represent some physical properties observed experimentally [9]. Several models that describe hysteresis can be found in the literature, for example, Presaich's model, Prandtl-Ishlinkiĭ [10] and the classic model proposed by Bouc (1971) [11] and expanded by Wen (1976) [12]. Unfortunately, few research works have used white-box modelling to derive analytical solutions for hysteretic systems, and contributions still lack in the literature.

For applications in a Bouc-Wen model, Okuizumi et al. (2004) [13] examined the response from a Bouc-Wen oscillator through the multiple scales method to verify the stability of the solutions by visualizing the trajectories on the phase plane. The idea behind the method lies on smoothing the hysteresis loop by an expansion of the restoring force using power series through multiple scales. Ikhouane and Rodellar (2005) [14] proposed the analytical characterization of the limit cycle that

* Corresponding author.
*E-mail addresses:* rafael.teloli@unesp.br (Rafael de O. Teloli), samuel.silva13@unesp.br (S. da Silva).

https://doi.org/10.1016/j.ymssp.2018.11.044
0888-3270/

occurs in Bouc-Wen oscillator for a periodic input by using its normalized version and instrumental functions that can describe the effect of parameters of the model on the hysteresis loop. Other works use equivalent linearization to achieve analytic expressions for the oscillator response, such as Shen et al. (2005) [15], who used the averaging method to obtain the response of a suspension system with a magnetorheological damper, and Jalali (2014) [16], who proposed an alternative linearized approach to deal with weakly hysteretic systems.

In addition, the multidimensional Fourier transform of the Volterra kernels, so-called higher-order FRFs and computed through the classical harmonic probing method, is an attractive white-box modelling approach widely used in structural dynamics for nonlinear modal analysis [17,18], system identification problems [19–22], output-only applications [23], structural damage assessment [24] and so on [25]. Furthermore, if it were not for technical limitations, such as the presence of module functions in most examples involving hysteresis and the fading memory property that exists in the Volterra series [26], the methodology could be an interesting tool to deal with hysteretic systems by deriving analytical expressions that approach in an approximate way the hysteresis loop.

Therefore, to apply the Volterra theory to evaluate hysteretic systems, the nonlinear restoring force needs to be previously smoothed by some procedure. Ran et al. (2014) [27] proposed simplifying assumptions that allowed to smooth the restoring force of a hysteretic system modeled by the Bouc-Wen model by using Taylor series, but the hysteretic loop was not reproduced. Manson and Worden (2016) [28] explored the possibility of considering the non-smooth system as a combination of smooth systems to develop a Volterra series representation for such models. That method aims to rewrite motion equations by removing the hysteretic effect using a switch between the smoothed submodels. Unfortunately, it was also not possible to represent analytically the hysteresis loop using the Volterra series since the switching procedure among the submodels includes a transient component in the total output.

In summary, the main drawbacks listed in applying the Volterra theory to deal with hysteretic systems arise from the procedure performed to smooth the hysteretic restoring force. Thus, the contribution of the present paper to overcome this technical limitation lies on using a smooth nonlinear operator based on bounding functions that aim to reproduce individually the loading and unloading regime of the restoring force in systems that carry the rate-independent hysteresis property. Since the polynomial form of the bounding functions can smooth properly the hysteretic restoring force, the novelty of this paper is to identify parametrically, by using a harmonic probing algorithm, the higher-order frequency response functions of an equivalent system that has the nonlinear operator. Although the results obtained here allow the hysteresis loop for narrow-banded input conditions to be represented analytically, to the best of our knowledge, the possibility of describing an analytical hysteresis loop approached by Volterra model was not demonstrated in previous works.

The paper is organized in 5 sections. First, Section 2 shows the assumptions used to develop the smooth bounding functions. Section 3 introduces the Volterra theory and the harmonic probing method employed to derive analytical expressions for the higher-order frequency response functions. Next, Section 4 presents the numerical application of the suggested approach for the Bouc-Wen model benchmark recently proposed by Noël and Shoukens (2016) [29] at the Workshop on Nonlinear System Identification Benchmarks. Further details about the challenges involving the hysteretic benchmark are also enlightened by Esfahani et al. (2018) [30], Bajrić and Høgsberg (2018) [31], Rebillat and Schoukens (2018) [32], and Worden et al. (2018) [33]. Finally, Section 5 reports the final remarks and the next steps for future works.

## 2. On the smooth nonlinear operator

Nonlinear operators can be used to describe non-smooth systems or even singular functions [34–37]. Giri et al. (2014) [38] demonstrated that effects of backlash presented in non-smooth oscillators can be approached through Wiener models by applying beforehand a piecewise smooth operator. Radouane et al. (2017) [39] assume a similar procedure to analyze a hysteretic system modeled by a Bouc-Wen oscillator. Martins and Aguirre (2016) [40] discussed sufficient conditions to identify autoregressive models for rate-independent hysteretic systems to reproduce multiple solutions in the polynomial model by considering a single-input and single-output (SISO) Hammerstein model, which uses a multi-input and single-output (MISO) deterministic NARX block. It is important to point out that all these bounding functions or structures do not try to propose new physical models, but rather to extend methods and techniques to deal with non-smooth systems. In addition, the present paper relates the Bouc-Wen parameters to the polynomial coefficients that compose the bounding functions, as it is shown in 2.2.

### 2.1. Nonlinear operator

Some assumptions need to be made. First, a system with hysteresis that carries the bounded-input bounded-output (BIBO) property when excited by a harmonic input $u(t) = A\cos(\omega t)$ bounded between amplitudes $-\infty < -A \leqslant u(t) \leqslant A < \infty$ will produce on the displacement $\times$ restoring force plane a hysteresis loop delimited by the enclosed area *ABCD* [1], as is shown in Fig. 1(a).

The excitation $u(t)$ belongs to the class of $T-$periodic input signals [9] and presents a periodic loading–unloading regime defined in a period $T \in \mathrm{IR}^{+}$. Thus, the output from the hysteretic system $-\infty < y_{\min} \leqslant y(t) \leqslant y_{\max} < \infty$ moves along two different paths. When $\dot{u}(t) > 0$ the output $y(t)$ is subjected to the load regime in the interval $y^{\uparrow}(t) \in [y(t+mT), \quad y(t+(m+\kappa)T)]$ and the pair $(\mathcal{Z}, y)$ moves along the path *BCA*. On the other hand, when $\dot{u}(t) < 0$, the

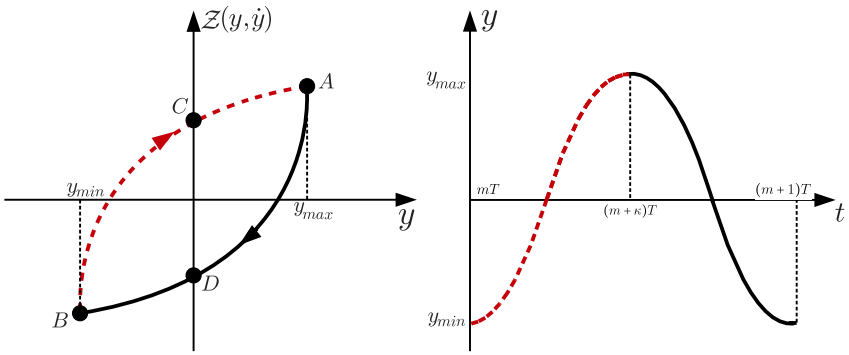


(a) Hysteresis loop. (b) Hysteretic response.

**Fig. 1.** Example of hysteresis loop in time continuous domain for a bounded loading–unloading input. – – – is the loading output and – the unloading output.

system is in the unloading regime in the interval $y^{\downarrow}(t) \in [y(t+(m+\kappa)T), \quad y(t+(m+1)T)]$ and the pair $(\mathcal{Z}, y)$ moves along *ADB*, where $\kappa = \frac{1}{2}$ is a time constant and $m \in \mathbb{Z}^+$ is the number of oscillation cycles. This second remark was well discussed by Radouane et al. (2017) [39] for defining the hysteretic loop assumption. Furthermore, systems where the restoring force $\mathcal{Z}$ encodes the hysteresis depending only on the $y_{\min} \leqslant y(t) \leqslant y_{\max}$ excursion interval are called rate-independent hysteretic systems. The Bouc-Wen, Duhem, Presaich, Prandtl-Ishlinkii models, etc. exhibit this property [10].

From the description of the loading–unloading paths on the hysteresis loop, it is possible to propose the bounding functions making use of the Weierstrass approximation theorem [41], which defines if $f(x)$ is a continuous function defined in the interval $[A, B]$ and, if an approximation error $\epsilon > 0$ exists, then a polynomial form $P(x)$ in $[A, B]$ exists such that:

$$|f(x) - P(x)| < \epsilon \quad \forall\, x \in [A, B] \tag{1}$$

Assuming that the load and unload regime cycles on the hysteresis loop can be interpreted individually, one can propose a particular function for each regime by encoding its nonlinear dynamic to transform a hysteretic system into an equivalent piecewise smooth problem.

Then, let $\mathcal{F}^{\uparrow}[y(t)]$ and $\mathcal{F}^{\downarrow}[y(t)]$ be continuous bounding functions along the interval $y_{\min} \leqslant y(t) \leqslant y_{\max}$ to describe properly the load and unload regimes, respectively. Based on the Weierstrass approximation theorem, the functions $\mathcal{F}^{\uparrow}[y(t)]$ and $\mathcal{F}^{\downarrow}[y(t)]$ can be written as [38]:

$$\mathcal{F}[y(t)] : \begin{cases} \mathcal{F}^{\uparrow}[y(t)] = f_0 + f_1 y(t) + \cdots + f_n y^n(t) & \text{for} \quad \text{sign}\ (\dot{u}(t)) \geqslant 0 \\ \mathcal{F}^{\downarrow}[y(t)] = d_0 + d_1 y(t) + \cdots + d_n y^n(t) & \text{for} \quad \text{sign}\ (\dot{u}(t)) \leqslant 0 \end{cases} \tag{2}$$

where $f_0 + f_1 + \cdots + f_n$ and $d_0 + d_1 + \cdots + d_n$ are the coefficients that compose the bounding functions. Furthermore, the continuity relation between these functions must be guaranteed to provide a smooth transition between the cycles:

$$\begin{aligned} \mathcal{F}^{\uparrow}[y(t+mT)] &= \mathcal{F}^{\downarrow}[y(t+mT)] \\ \mathcal{F}^{\uparrow}[y(t+(m+\kappa)T)] &= \mathcal{F}^{\downarrow}[y(t+(m+\kappa)T)] \forall t \end{aligned} \tag{3}$$

After establishing the existence of bounding functions, the next section presents how to rewrite the coefficients $f_0 + f_1 + \cdots + f_n$ and $d_0 + d_1 + \cdots + d_n$ as a function of the hysteretic system described by the Bouc-Wen model.

### 2.2. Application example on the Bouc-Wen oscillator

The classic phenomenological oscillator model proposed by Bouc (1967) [42] and expanded by Wen (1976) [12] to describe a single-degree-of-freedom system with hysteresis is given by:

$$m\ddot{y}(t) + c\dot{y}(t) + ky(t) + \mathcal{Z}(y,\dot{y}) = u(t) \tag{4}$$

$$\dot{\mathcal{Z}}(y,\dot{y}) = \alpha\dot{y}(t) - \beta\Big(\gamma|\dot{y}(t)||\mathcal{Z}(y,\dot{y})|^{\nu-1}\mathcal{Z}(y,\dot{y}) + \delta\dot{y}(t)|\mathcal{Z}(y,\dot{y})|^{\nu}\Big) \tag{5}$$

where $m$ [kg] is the mass, $c$ [Ns/m] is the viscous damping, $k$ [N/m] is the linear stiffness, $\alpha$ [N/m], $\beta, \gamma$ [$m^{-1}$], $\delta$ [$m^{-1}$] and $\nu$ are the Bouc-Wen parameters. In addition, $\ddot{y}, \dot{y}$ and $y$ are the acceleration [$m/s^2$], velocity [m/s] and displacement [m], respectively, for an excitation input $u$ [N]. The term $\mathcal{Z}(y,\dot{y})$ represents the hysteretic force that is described by the ordinary differential equation $\dot{\mathcal{Z}}(y,\dot{y})$.

In fact, the use of the Volterra series and the harmonic probing method in Eqs. (4) and (5) is not possible due to the presence of absolute values. However, the smooth bounding functions $\mathcal{F}^{\uparrow}[y(t)]$ and $\mathcal{F}^{\downarrow}[y(t)]$ can be well represented by the Volterra series, since their representation are convergent. In this way, the interest in proposing the nonlinear operator is to explore the possibility of the higher-order FRFs describing systems with hysteresis in addition to being parametrized by the Bouc-Wen parameters.

The shape of the hysteresis loop changes according to the model parameters and more details are given by [14,43–45]. Dividing the Eq. (5) by $\dot{y}$:

$$\begin{aligned} &\frac{d\mathcal{Z}}{dy} = \alpha - \beta\left(\frac{\gamma|\dot{y}||\mathcal{Z}|^{\nu-1}\mathcal{Z}}{\dot{y}} + \delta|\mathcal{Z}|^{\nu}\right) \\ \Rightarrow \quad &\frac{d\mathcal{Z}}{dy} = \alpha - \beta|\mathcal{Z}|^{\nu}[\mathrm{sgn}(\dot{y}\mathcal{Z})\gamma + \delta] \end{aligned} \tag{6}$$

If $\mathcal{Z} = 0$, the slope of the restoring force is $\alpha$ implying that the parameter $\alpha$ can be associated in an equivalent way with the linear stiffness $k$ when the oscillator is subjected to null initial conditions. Moreover, it is important to point out that $\beta$ is responsible for the hysteresis effects, $\gamma$ in turn, whose values are always greater than zero for real systems, is the parameter that controls the hysteretic relationship between $\mathcal{Z}$ and $y$. Finally, the combination of $(\pm\gamma + \delta)$ characterizes the hardening or softening behavior in the hysteresis loop [46].

The explicit time integration of Eq. (6) with $\nu = 1$ divides the hysteresis loop of the Bouc-Wen model into four different intervals on the force $\times$ displacement plan between the signs of $\dot{y}$ and $\mathcal{Z}$. The equations of each interval are given by:

- Interval (i): $\dot{y} \leqslant 0, \mathcal{Z} \geqslant 0$

$$\mathcal{Z}_1 = \frac{\alpha}{\beta(\delta-\gamma)}\left(1 - e^{-\beta(\delta-\gamma)(y-y_0)}\right) \tag{7}$$

- Interval (ii): $\dot{y} \leqslant 0, \mathcal{Z} \leqslant 0$

$$\mathcal{Z}_2 = -\frac{\alpha}{\beta(\delta+\gamma)}\left(1 - e^{\beta(\delta+\gamma)(y-y_0)}\right) \tag{8}$$

- Interval (iii): $\dot{y} \geqslant 0, \mathcal{Z} \leqslant 0$

$$\mathcal{Z}_3 = -\frac{\alpha}{\beta(\delta-\gamma)}\left(1 - e^{\beta(\delta-\gamma)(y+y_0)}\right) \tag{9}$$

- Interval (iv): $\dot{y} \geqslant 0, \mathcal{Z} \geqslant 0$

$$\mathcal{Z}_4 = \frac{\alpha}{\beta(\delta+\gamma)}\left(1 - e^{-\beta(\delta+\gamma)(y+y_0)}\right) \tag{10}$$

where $y_0$ is the displacement at $\mathcal{Z} = 0$. The loading regime of the hysteresis cycle is described by the pair $(\mathcal{Z}_3, \mathcal{Z}_4)$, whereas that the unload pair is $(\mathcal{Z}_1, \mathcal{Z}_2)$. Besides that, these equations can check when $y_0$ assumes a unique absolute value in Eqs. (7)–(10), since the hysteresis loop of the oscillator is symmetric regarding each regime of motion. Under these conditions, the bounding functions need to have the same structure for load and unload cycles, which means that the coefficients with the same subscript have equal absolute values, i. e., $f_0 = d_0, f_1 = d_1, \ldots f_n = d_n$.

An alternative way to rewrite the restoring force Eqs. (7)–(10) is by using the Taylor series approach around the displacement $y_0$ assuming the first three orders:

$$\mathcal{Z}_1 = \alpha(y-y_0) - \frac{\alpha\beta(\delta-\gamma)}{2}(y-y_0)^2 + \frac{\alpha(-\beta(\delta-\gamma))^2}{6}(y-y_0)^3 \tag{11}$$

$$\mathcal{Z}_2 = \alpha(y-y_0) + \frac{\alpha\beta(\delta+\gamma)}{2}(y-y_0)^2 + \frac{\alpha(\beta(\delta+\gamma))^2}{6}(y-y_0)^3 \tag{12}$$

$$\mathcal{Z}_3 = \alpha(y+y_0) + \frac{\alpha\beta(\delta-\gamma)}{2}(y+y_0)^2 + \frac{\alpha(\beta(\delta-\gamma))^2}{6}(y+y_0)^3 \tag{13}$$

$$\mathcal{Z}_4 = \alpha(y+y_0) - \frac{\alpha\beta(\delta+\gamma)}{2}(y+y_0)^2 + \frac{\alpha(-\beta(\delta+\gamma))^2}{6}(y+y_0)^3 \tag{14}$$

Logically, the more terms included in the Taylor series approach, the greater the precision of the polynomial form for the hysteresis loop will be. However, for sake of simplicity and by convergence assurance for the conditions addressed in this work, the functions $\mathcal{F}^{\downarrow}[y(t)]$ and $\mathcal{F}^{\uparrow}[y(t)]$ assume a polynomial form up to the cubic term according to the order used in the Taylor series approach:

$$\mathcal{F}^{\uparrow}[y(t)] = \lambda_0 + \lambda_1 y(t) - \lambda_2 y^2(t) + \lambda_3 y^3(t) \text{ for sign } (\dot{u}(t)) \geqslant 0 \tag{15}$$

$$\mathcal{F}^{\downarrow}[y(t)] = -\lambda_0 + \lambda_1 y(t) + \lambda_2 y^2(t) + \lambda_3 y^3(t) \text{ for sign}(\dot{u}(t)) \leqslant 0 \tag{16}$$

where $\lambda_0$ [N], $\lambda_1$ [N/m], $\lambda_2$ [N/m$^2$] and $\lambda_3$ [N/m$^3$] are their coefficients. Also, each coefficient is responsible for describing many features of the hysteresis loop, for instance, $\lambda_0$ provides the multiple solutions to the nonlinear operator, $\lambda_1$ is the slope of the restoring force and finally, $\lambda_2$ and $\lambda_3$ give the hardening or softening stiffness characteristics to the model. Comparing Eqs. (11)–(14), the $\mathcal{F}^{\downarrow}[y(t)]$ is used to approach the pair $\mathcal{Z}_1$ and $\mathcal{Z}_2$, which describes the intervals (i) and (ii), whereas the $\mathcal{F}^{\uparrow}[y(t)]$ function is responsible for the other ones. Finally, the motion equation using the proposed nonlinear operator is given by:

$$m\ddot{y}(t) + c\dot{y}(t) + ky(t) + \mathcal{F}[y(t)] = u(t) \tag{17}$$

The coefficients of the polynomial form are computed by minimizing an error function described by [21]:

$$E(\lambda_0, \lambda_1, \lambda_2, \lambda_3) = \int_{-Y}^{y_0} \left\{\mathcal{Z}_2 - \mathcal{F}^{\downarrow}[y(t)]\right\}^2 dy + \int_{y_0}^{Y} \left\{\mathcal{Z}_1 - \mathcal{F}^{\downarrow}[y(t)]\right\}^2 dy \tag{18}$$

subjected to:

$$\frac{\partial E}{\partial \lambda_i} = 0, \quad \text{for } i = 0, 1, 2, 3 \tag{19}$$

which results in the following expressions:

$$\lambda_0 = \frac{\alpha y_0}{16}(3\beta\delta Y + 8\beta\gamma y_0 - 16) \tag{20}$$

$$\lambda_1 = \alpha \tag{21}$$

$$\lambda_2 = \frac{\alpha\beta}{16Y}(8\beta\delta^2 Y y_0 + 8\beta\gamma^2 Y y_0 + 15\beta\delta\gamma y_0^2 - 8\gamma Y - 15\delta y_0) \tag{22}$$

$$\lambda_3 = \frac{\alpha\beta}{96Y^5}\left(\begin{array}{c} 16\beta\delta^2 Y^5 + 70\beta\delta\gamma Y^4 y_0 - 70\beta\delta\gamma Y^2 y_0^3 - 35\delta Y^4 + \\ 105\delta Y^2 y_0^2 - 105\delta y_0^4 \end{array}\right) \tag{23}$$

where $Y = |y_{\min}| = |y_{\max}|$. These equations are valid only for harmonic excitations that ensure a weak hysteretic force and when the force $\times$ displacement plane draws a single loop. Furthermore, despite the application illustrated on a Bouc-Wen model, the approach proposed could be used to deal with other hysteretic systems with the rate-independent property.

## 3. Multi-input Volterra series and the Harmonic Probing Method

For multi-input and single-output (MISO) systems, the functional of the Volterra series in continuous time domain is given by the following mapping with the multi-inputs $u_1(t) + u_2(t) + \cdots + u_j(t)$ [47]:

$$\begin{aligned} y(t) = \sum_{\eta=1}^{\infty} y_\eta(t) = & \underbrace{\sum_{p=1}^{j} \int_{\mathrm{IR}^1} h_1^{(u_p)}(\tau_1) u_p(t-\tau_1) d\tau_1}_{=y_1(t)} \\ & + \underbrace{\sum_{p=1}^{j}\sum_{k=1}^{j} \int_{\mathrm{IR}^2} h_2^{(u_p,u_k)}(\tau_1,\tau_2) u_p(t-\tau_1) u_k(t-\tau_2) d\tau_1 d\tau_2}_{=y_2(t)} \\ & + \underbrace{\sum_{p=1}^{j}\sum_{k=1}^{j}\sum_{l=1}^{j} \int_{\mathrm{IR}^3} h_3^{(u_p,u_k,u_l)}(\tau_1,\tau_2,\tau_3) u_p(t-\tau_1) u_k(t-\tau_2) u_l(t-\tau_3) d\tau_1 d\tau_2 d\tau_3}_{=y_3(t)} \\ & \text{and higher} - \text{order contributions} \end{aligned} \tag{24}$$

where each polynomial contribution of $\eta-$order is given by:

$$y_\eta(t) = \sum_{p=1}^{j}\sum_{k=1}^{j} \cdots \sum_{n=1}^{j} \int_{\mathrm{IR}^\eta} h_\eta^{(u_p,u_k,\ldots,u_n)}(\tau_1,\tau_2,\ldots,\tau_\eta) \prod_{i=1}^{\eta} u_p(t-\tau_1) u_k(t-\tau_2) \ldots u_n(t-\tau_\eta) d\tau_1 d\tau_2 \ldots d\tau_\eta \tag{25}$$

The term $h_{\eta}^{(u_p,u_k,\ldots,u_n)}(\tau_1,\tau_2,\ldots,\tau_\eta)$ is called direct or cross Volterra kernel related to the $j^{\text{th}}$ input and is a generalization of the well-known impulse response function [23]. In order to simplify the notation it is assumed that:

$$\int_{\mathrm{IR}^\eta} = \int_{\mathrm{IR}\times\mathrm{IR}\times\ldots\mathrm{IR}} = \underbrace{\int_{-\infty}^{\infty}\int_{-\infty}^{\infty}\cdots\int_{-\infty}^{\infty}}_{\eta\text{th order}}$$

The estimation of each contribution for a MISO system involves a large number of parameters that occur over-parametrization. However, these kernels can be constructed in a symmetric way, which reduces the number of terms to be calculated [48], i. e., the term $h_{\eta}^{(u_1,u_2,\ldots,u_m)}(\tau_1,\tau_2,\ldots,\tau_\eta)$ is considered identical for all the input permutations, for instance $h_2^{(u_1,u_2)}(\tau_1,\tau_2) = h_2^{(u_2,u_1)}(\tau_1,\tau_2)$. Then, assuming $m=2$ the contributions are given by:

$$\begin{aligned} &y_1(t) = y_1^{(u_1)}(t) + y_1^{(u_2)}(t) \\ &\Longleftrightarrow y_1(t) = \textstyle\int_{\mathrm{IR}^1} h_1^{(u_1)}(\tau_1)u_1(t-\tau_1)d\tau_1 + \\ &\quad \textstyle\int_{\mathrm{IR}^1} h_1^{(u_2)}(\tau_1)u_2(t-\tau_1)d\tau_1 \end{aligned} \tag{26}$$

$$\begin{aligned} &y_2(t) = y_2^{(u_1,u_1)}(t) + y_2^{(u_2,u_2)}(t) + y_2^{(u_1,u_2)}(t) \\ &\Longleftrightarrow y_2(t) = \textstyle\int_{\mathrm{IR}^2} h_2^{(u_1,u_1)}(\tau_1,\tau_2)u_1(t-\tau_1)u_1(t-\tau_2)d\tau_1d\tau_2 + \\ &\quad \textstyle\int_{\mathrm{IR}^2} h_2^{(u_2,u_2)}(\tau_1,\tau_2)u_2(t-\tau_1)u_2(t-\tau_2)d\tau_1d\tau_2 + \\ &\quad 2\textstyle\int_{\mathrm{IR}^2} h_2^{(u_1,u_2)}(\tau_1,\tau_2)u_1(t-\tau_1)u_2(t-\tau_2)d\tau_1d\tau_2 \\ &\quad + \text{higher} - \text{order contributions} \end{aligned} \tag{27}$$

The higher-order FRFs, as well as the linear FRFs, provide an interesting insight into the dynamical properties of nonlinear systems in the frequency domain [49]. It is important to point out that since the higher-order FRFs are known, these functions can be used to describe the system output for any input with a well-known mathematical expression. The multi-dimensional Fourier transform of the Volterra kernels for multi-inputs can be calculated by [50,51]:

$$\mathcal{H}_{\eta}^{(u_p,u_k,\ldots,u_n)}(\omega_1,\omega_2,\cdots,\omega_\eta) = \int_{\mathrm{IR}^\eta} h_{\eta}^{(u_p,u_k,\ldots,u_n)}(\tau_1,\tau_2,\ldots,\tau_\eta)\times\prod_{i=1}^{\eta}e^{-j\omega_i\tau_i}d\tau_1d\tau_2\ldots\tau_\eta \tag{28}$$

The computation of the higher-order FRFs carried out through the harmonic probing method requires knowledge of the motion equations such as white-box modelling. For a three-tone input given by:

$$\begin{aligned} u(t) = &\ A\cos\omega_1 t + B\cos\omega_2 t + C\cos\omega_3 t \\ \Rightarrow u(t) = &\ \tfrac{A\left(e^{j\omega_1 t}+e^{-j\omega_1 t}\right)}{2} + \tfrac{B\left(e^{j\omega_1 t}+e^{-j\omega_1 t}\right)}{2} + \tfrac{C\left(e^{j\omega_1 t}+e^{-j\omega_1 t}\right)}{2} \end{aligned} \tag{29}$$

the generalized expression for the contributions mapping of $\eta-$order is written as [20]:

$$y_\eta(t) = \frac{1}{2^\eta}\sum_{N+M+L=\eta} A^N B^M C^L\left(C_{p,q,r,s,v,\varpi}^{\eta}\right)\mathcal{H}_{\eta}^{p,q,r,s,v,\varpi}(\omega)e^{j(N\omega_1+M\omega_2+L\omega_3)t} \tag{30}$$

where $p,q,r,s,v$ and $\varpi$ are integer values and

$$C_{p,q,r,s,v,\varpi}^{\eta} = \frac{\eta}{p!q!r!s!v!\varpi!} \tag{31}$$

$$\mathcal{H}_{\eta}^{p,q,r,s,v,\varpi}(\omega) = \mathcal{H}_\eta\left(\underbrace{\omega_1,\ldots,\omega_1}_{p\text{ times}},\underbrace{-\omega_1,\ldots,-\omega_1}_{q\text{ times}},\underbrace{\omega_2,\ldots,\omega_2}_{r\text{ times}},\underbrace{-\omega_2,\ldots,-\omega_2}_{s\text{ times}},\underbrace{\omega_3,\ldots,\omega_3}_{v\text{times}},\underbrace{-\omega_3,\ldots,-\omega_3}_{\varpi\text{ times}}\right) \tag{32}$$

With the generalized series response established for a multi-input case, it is possible to derive the higher-order FRFs for the motion Eq. (17) described by the nonlinear operator as an equivalent hysteretic system.

### 3.1. Higher-order FRFs applied on the nonlinear operator

The equivalent system with hysteresis defined in Eq. (17) carries the change between the bounding functions according to $\text{sign}[\dot{u}(t)]$, which can be approximated well by a square wave with the same period of $\dot{u}(t)$. Thus, Eq. (17) can be rewritten as:

$$m\ddot{y}(t) + c\dot{y}(t) + ky(t) + \underbrace{u_0(t) + \lambda_1 y(t) + \varrho y^2(t) + \lambda_3 y^3(t)}_{=\mathcal{F}[y(t)]} = u(t) \tag{33}$$

where the term $u_0(t) = \lambda_0 \Phi[\dot{u}(t)]$, with $\Phi[\dot{u}(t)] \approx \text{sign}[\dot{u}(t)]$, is considered as an additional input applied to the equivalent system and $\varrho$ is defined as $\varrho = \lambda_2$ ($\varrho = -\lambda_2$) for $\text{sgn}[\dot{u}(t)] < 0 (\text{sgn}[\dot{u}(t)] > 0)$.

Since the nonlinear operator has terms up to the cubic order, it is used $m = 3$ contributions to compute the higher-order FRFs. More than three contributions could be used to predict the output, but the complexity to compute other higher-order FRFs kernels is increased. Fortunately, as highlighted by Lin and Ng (2018) [22], the use of the first three Volterra kernels has been suitable to deal with polynomial nonlinearities similar to that presented in the Eq. (33), as well as in practical engineering problems [52].

The discontinuity that occurs with $\varrho y^2(t)$ directly impacts on the calculation of the second order Volterra contribution in the time domain; however, as pointed out in Section 3.2 the discontinuity can be overcome. The changes on $\Phi[\bullet]$ can be described by Fourier series:

$$\begin{aligned} u_0(t) &= \lambda_0 \underbrace{\sum_{k=1}^{N_s} \frac{4 \sin\{[1+2(k-1)]\omega t\}}{[1+2(k-1)]\pi}}_{=\Phi[\dot{u}(t)]} \\ \iff u_0(t) &= \frac{j2\lambda_0}{\pi} \underbrace{\sum_{k=1}^{N_s} \left( \frac{e^{-j[1+2(k-1)]\omega t} - e^{j[1+2(k-1)]\omega t}}{1+2(k-1)} \right)}_{=\Phi[\dot{u}(t)]} \\ \Rightarrow u_0(t) &= \sum_{k=1}^{N_s} A_k \left( e^{j[1+2(k-1)])\omega t} - e^{-j[1+2(k-1)]\omega t} \right) \end{aligned} \tag{34}$$

where

$$A_k = -\frac{j2\lambda_0}{\pi + 2(k-1)\pi} \tag{35}$$

and $\omega$ is the excitation frequency [rad/s], $N_s$ is the number of terms used by the Fourier series and $j = \sqrt{-1}$. This approximation states that: if $N_s$ tends to $\infty$, then $\Phi[\dot{u}(t)]$ must tends to $\text{sign}[\dot{u}(t)]$. Thus, for a single-tone input $u(t) = Ae^{j\omega t}$ the following additional input is assumed with $N_s = 2$:

$$u_0(t) = A_1 e^{j\omega t} + A_2 e^{j3\omega t} \tag{36}$$

The calculation of the higher-order FRF is carried out by assuming the probing harmonic inputs:

$$u_1 = Ae^{j\omega t} \qquad u_2 = A_1 e^{j\omega t} \qquad u_3 = A_2 e^{j3\omega t} \tag{37}$$

based on the generalized response contributions, the probing expressions of displacement, velocity and acceleration for the first order $y_1(t)$ contribution are:

$$\begin{aligned} y_1 &= A\mathcal{H}_1^{(u_1)}(\omega)e^{j\omega t} + A_1\mathcal{H}_1^{(u_2)}(\omega)e^{j\omega t} + A_2\mathcal{H}_1^{(u_3)}(3\omega)e^{j3\omega t} \\ \dot{y}_1 &= j\omega A\mathcal{H}_1^{(u_1)}(\omega)e^{j\omega t} + j\omega A_1\mathcal{H}_1^{(u_2)}(\omega)e^{j\omega t} + j3\omega A_2\mathcal{H}_1^{(u_3)}(3\omega)e^{j3\omega t} \\ \ddot{y}_1 &= -\omega^2 A\mathcal{H}_1^{(u_1)}(\omega)e^{j\omega t} - \omega^2 A_1\mathcal{H}_1^{(u_2)}(\omega)e^{j\omega t} - (3\omega)^2 A_2\mathcal{H}_1^{(u_3)}(3\omega)e^{j3\omega t} \end{aligned} \tag{38}$$

by substituting the responses into Eq. (33), and equating the terms $Ae^{j\omega t}, A_1 e^{j\omega t}, A_2 e^{j3\omega t}$ provides:

$$\mathcal{H}_1^{(u_1)}(\omega) = \mathcal{H}_1^{(u_2)}(\omega) = \mathcal{H}_1(\omega) \iff \mathcal{H}_1(\omega) = \frac{1}{-m\omega^2 + j\omega c + (k+\lambda_1)} \tag{39}$$

$$\mathcal{H}_1^{(u_3)}(3\omega) = \mathcal{H}_1(3\omega) \iff \mathcal{H}_1(3\omega) = \frac{1}{-m(3\omega)^2 + j3\omega c + (k+\lambda_1)} \tag{40}$$

the kernel expression $\mathcal{H}_1(\omega)$ corresponds to the linear FRF, where $\omega_n = \sqrt{(k+\lambda_1)m^{-1}}$. The first order contribution $y_1(t)$ holds the superposition principle and, for this reason, its kernel $\mathcal{H}_1^{(u_3)}(3\omega)$ presents resonance frequency at $3\omega = \omega_n \Rightarrow \omega = \omega_n/3$ due to the harmonic from the input signal $e^{j3\omega t}$. Furthermore, the kernels that have been derived by the single-tone inputs $u_1 = Ae^{j\omega t}$ and $u_2 = A_1 e^{j\omega t}$will always show equal expressions for both inputs, for instance $\mathcal{H}_2^{u_1,u_1}(\omega_1,\omega_2) = \mathcal{H}_2^{u_2,u_2}(\omega_1,\omega_2) = \mathcal{H}_2^{u_1,u_2}(\omega_1,\omega_2)$. For this reason, the kernel superscripts are omitted as well as the computation of the kernels that arise from the input $u_2$.

The mapping performed through the nonlinear contributions in the frequency domain requires that the kernel transforms contains a sum of frequency components $(\omega_1 + \omega_2)$ and $(\omega_1 + \omega_2 + \omega_3)$ for the second and third order contributions, respectively. Moreover, the algorithm developed by Worden et al. (1997) [50] computes the higher-order kernels to analyze

separately each term that composes the contribution $y_\eta(t)$. This procedure uses a significant reduction of the mathematical effort to obtain the kernels. The probing inputs to estimate the second order direct-kernels are given by:

$$u_1 = Ae^{j\omega_1 t} + Ae^{j\omega_2 t}, \qquad u_3 = A_2 e^{j3\omega_1 t} + A_2 e^{j3\omega_2 t} \tag{41}$$

then, the responses $y_2^{(u_1,u_1)}, \dot{y}_2^{(u_1,u_1)}$ and $\ddot{y}_2^{(u_1,u_1)}$ are:

$$\begin{aligned} y_2^{(u_1,u_1)} &= A\mathcal{H}_1(\omega_1)e^{j\omega_1 t} + A\mathcal{H}_1(\omega_2)e^{j\omega_2 t} + 2A^2\mathcal{H}_2(\omega_1,\omega_2)e^{j(\omega_1+\omega_2)t} \\ \dot{y}_2^{(u_1,u_1)} &= j\omega_1 A\mathcal{H}_1(\omega_1)e^{j\omega_1 t} + j\omega_2 A\mathcal{H}_1(\omega_2)e^{j\omega_2 t} + j2(\omega_1+\omega_2)A^2\mathcal{H}_2(\omega_1,\omega_2)e^{j(\omega_1+\omega_2)t} \\ \ddot{y}_2^{(u_1,u_1)} &= -\omega_1^2 A\mathcal{H}_1(\omega_1)e^{j\omega_1 t} - \omega_2^2 A\mathcal{H}_1(\omega_2)e^{j\omega_2 t} - 2(\omega_1+\omega_2)^2 A^2\mathcal{H}_2(\omega_1,\omega_2)e^{j(\omega_1+\omega_2)t} \end{aligned} \tag{42}$$

substituting the expressions (42) into Eq. (33) and equating the terms $A^2 e^{j(\omega_1+\omega_2)t}$ the second order Volterra direct-kernel is given by:

$$\mathcal{H}_2(\omega_1,\omega_2) = -\varrho\mathcal{H}_1(\omega_1)\mathcal{H}_1(\omega_2)\mathcal{H}_1(\omega_1+\omega_2) \tag{43}$$

Applying the previous procedure with the outputs $y_2^{(u_2,u_2)}, \dot{y}_2^{(u_2,u_2)}$ and $\ddot{y}_2^{(u_2,u_2)}$ yields:

$$\mathcal{H}_2(3\omega_1,3\omega_2) = -\varrho\mathcal{H}_1(3\omega_1)\mathcal{H}_1(3\omega_2)\mathcal{H}_1(3\omega_1+3\omega_2) \tag{44}$$

To obtain the simplified mapping for the second order Volterra cross-kernel, the probing is performed with the inputs $u_1 = Ae^{j\omega_1 t}$ and $u_2 = A_2 e^{j3\omega_2 t}$. Thus, the output probing expression is given by:

$$\begin{aligned} y_2^{(u_1,u_2)} &= A\mathcal{H}_1(\omega_1)e^{j\omega_1 t} + A_2\mathcal{H}_1(3\omega_2)e^{j3\omega_2 t} + 2AA_2\mathcal{H}_2(\omega_1,3\omega_2)e^{j(\omega_1+3\omega_2)t} \\ \dot{y}_2^{(u_1,u_2)} &= j\omega_1 A\mathcal{H}_1(\omega_1)e^{j\omega_1 t} + j3\omega_2 A_2\mathcal{H}_1(3\omega_2)e^{j3\omega_2 t} + j2(\omega_1+3\omega_2)AA_2\mathcal{H}_2(\omega_1,3\omega_2)e^{j(\omega_1+3\omega_2)t} \\ \ddot{y}_2^{(u_1,u_2)} &= -\omega_1^2 A\mathcal{H}_1(\omega_1)e^{j\omega_1 t} - (3\omega_2)^2 A\mathcal{H}_1(3\omega_2)e^{j3\omega_2 t} - 2(\omega_1+3\omega_2)^2 AA_2\mathcal{H}_2(\omega_1,3\omega_2)e^{j(\omega_1+3\omega_2)t} \end{aligned} \tag{45}$$

The cross-kernel expression is:

$$\mathcal{H}_2(\omega_1,3\omega_2) = -\varrho\mathcal{H}_1(\omega_1)\mathcal{H}_1(3\omega_2)\mathcal{H}_1(\omega_1+3\omega_2) \tag{46}$$

All the second-order kernel expressions result in a three-dimensional plot figure. For this reason, the analysis of the surfaces is a difficult task, which can be overcome considering only the leading diagonal of the higher-order FRFs, since it provides the key features of the resonance peaks. For $\omega_1 = \omega_2 = \omega$, the leading diagonals are expressed as:

$$\mathcal{H}_2(\omega,\omega) = -\varrho\mathcal{H}_1^2(\omega)\mathcal{H}_1(2\omega), \tag{47}$$

$$\mathcal{H}_2(3\omega,3\omega) = -\varrho\mathcal{H}_1^2(3\omega)\mathcal{H}_1(6\omega), \tag{48}$$

$$\mathcal{H}_2(\omega,3\omega) = -\varrho\mathcal{H}_1(\omega)\mathcal{H}_1(3\omega)\mathcal{H}_1(4\omega) \tag{49}$$

As can be seen, all the second-order kernels are dependent on the loading–unloading cycles that occur along the hysteresis loop, since these kernels are affected by the changes on the parameter $\varrho$. When represented in time domain, the contribution $y_2(t)$ must be split into $y_2^{\downarrow}(t)$ and $y_2^{\uparrow}(t)$ derived by the kernels computed with $\varrho > 0$ and $\varrho < 0$, respectively. The harmonic interactions that occur between the frequency components from the inputs are clear in the cross-kernel $\mathcal{H}_2(\omega,3\omega)$, which shows sub-harmonics at frequencies of $3\omega$ and $4\omega$.

The third-order direct-kernels are derived from following probing inputs:

$$u_1 = Ae^{j\omega_1 t} + Ae^{j\omega_2 t} + Ae^{j\omega_3 t}, \quad u_3 = A_2 e^{j3\omega_1 t} + A_2 e^{j3\omega_2 t} + A_2 e^{j3\omega_3 t} \tag{50}$$

then, the output probing expression $y_3^{(u_1,u_1,u_1)}$ is given by:

$$\begin{aligned} y_3^{(u_1,u_1,u_1)} &= A\mathcal{H}_1(\omega_1)e^{j\omega_1 t} + A\mathcal{H}_1(\omega_2)e^{j\omega_2 t} + A\mathcal{H}_1(\omega_3)e^{j\omega_3 t} + \\ & 2A^2\mathcal{H}_2(\omega_1,\omega_2)e^{j(\omega_1+\omega_2)t} + 2A^2\mathcal{H}_2(\omega_1,\omega_3)e^{j(\omega_1+\omega_3)t} + \\ & 2A^2\mathcal{H}_2(\omega_2,\omega_3)e^{j(\omega_2+\omega_3)t} + 6A^3\mathcal{H}_3(\omega_1,\omega_2,\omega_3)e^{j(\omega_1+\omega_2+\omega_3)t} \end{aligned} \tag{51}$$

where the responses $\dot{y}_3^{(u_1,u_1,u_1)}$ and $\ddot{y}_3^{(u_1,u_1,u_1)}$ are the first and second derivatives of $y_3^{(u_1,u_1)}$ with respect to time. Substituting the response terms into Eq. (33), the algebraic expression for $\mathcal{H}_3(\omega_1,\omega_2,\omega_3)$is given by equating the terms $A^3 e^{j(\omega_1+\omega_2+\omega_3)t}$:

$$\begin{aligned} \mathcal{H}_3(\omega_1,\omega_2,\omega_3) &= \mathcal{H}_1(\omega_1)\mathcal{H}_1(\omega_2)\mathcal{H}_1(\omega_3)\mathcal{H}_1(\omega_1+\omega_2+\omega_3)\times \\ & \left[\tfrac{2\varrho^2}{3}\{\mathcal{H}_1(\omega_1+\omega_2)+\mathcal{H}_1(\omega_1+\omega_3)+\mathcal{H}_1(\omega_2+\omega_3)\}-\lambda_3\right] \end{aligned} \tag{52}$$

The third-order direct-kernel obtained through the probing with $y_3^{(u_2,u_2,u_2)}, \dot{y}_3^{(u_2,u_2,u_2)}$ and $\ddot{y}_3^{(u_2,u_2,u_2)}$ is:

$$\begin{aligned}\mathcal{H}_3(3\omega_1,3\omega_2,3\omega_3) &= \mathcal{H}_1(3\omega_1)\mathcal{H}_1(3\omega_2)\mathcal{H}_1(3\omega_3)\mathcal{H}_1(3\omega_1+3\omega_2+3\omega_3)\times \\ &\left[\tfrac{2\varrho^2}{3}\{\mathcal{H}_1(3\omega_1+3\omega_2)+\mathcal{H}_1(3\omega_1+3\omega_3)+\mathcal{H}_1(3\omega_2+3\omega_3)\}-\lambda_3\right]\end{aligned} \tag{53}$$

The third-order cross-kernel transform is derived with the probing inputs $u_1 = Ae^{j\omega_1 t} + Ae^{j\omega_2 t}$ and $u_3 = A_2 e^{j\omega_3 t}$. These inputs generate the following response expression:

$$\begin{aligned}&y_3^{(u_1,u_1,u_3)} = A\mathcal{H}_1(\omega_1)e^{j\omega_1 t} + A\mathcal{H}_1(\omega_2)e^{j\omega_2 t} + A_2\mathcal{H}_1(3\omega_3)e^{j3\omega_3 t} + \\ &2A^2\mathcal{H}_2(\omega_1,\omega_2)e^{j(\omega_1+\omega_2)t} + 2AA_2\mathcal{H}_2(\omega_1,\omega_3)e^{j(\omega_1+3\omega_3)t} + \\ &2AA_2\mathcal{H}_2(\omega_2,\omega_3)e^{j(\omega_2+3\omega_3)t} + 6A^2A_2\mathcal{H}_3(\omega_1,\omega_2,3\omega_3)e^{j(\omega_1+\omega_2+3\omega_3)t}\end{aligned} \tag{54}$$

substituting $y_3^{(u_1,u_1,u_3)}$ and its derivatives into (33) produces the FRF expression:

$$\begin{aligned}\mathcal{H}_3(\omega_1,\omega_2,3\omega_3) &= \mathcal{H}_1(\omega_1)\mathcal{H}_1(\omega_2)\mathcal{H}_1(3\omega_3)\mathcal{H}_1(\omega_1+\omega_2+3\omega_3)\times \\ &\left[\tfrac{2\varrho^2}{3}\{\mathcal{H}_1(\omega_1+\omega_2)+\mathcal{H}_1(\omega_1+3\omega_3)+\mathcal{H}_1(\omega_2+3\omega_3)\}-\lambda_3\right]\end{aligned} \tag{55}$$

Moreover, the third-order cross-kernel from the contribution $y_3^{(u_1,u_3,u_3)}$ is given by:

$$\begin{aligned}\mathcal{H}_3(\omega_1,3\omega_2,3\omega_3) &= \mathcal{H}_1(\omega_1)\mathcal{H}_1(3\omega_2)\mathcal{H}_1(3\omega_3)\mathcal{H}_1(\omega_1+3\omega_2+3\omega_3)\times \\ &\left[\tfrac{2\varrho^2}{3}\{\mathcal{H}_1(\omega_1+3\omega_2)+\mathcal{H}_1(\omega_1+3\omega_3)+\mathcal{H}_1(3\omega_2+3\omega_3)\}-\lambda_3\right]\end{aligned} \tag{56}$$

The algebraic expression of the third-order kernels can be reduced considering only the leading diagonals, expressed as

$$\mathcal{H}_3(\omega,\omega,\omega) = \mathcal{H}_1^3(\omega)\mathcal{H}_1(3\omega)\left[2\varrho^2\mathcal{H}_1(2\omega)-\lambda_3\right], \tag{57}$$

$$\mathcal{H}_3(3\omega,3\omega,3\omega) = \mathcal{H}_1^3(3\omega)\mathcal{H}_1(9\omega)\left[2\varrho^2\mathcal{H}_1(6\omega)-\lambda_3\right], \tag{58}$$

$$\mathcal{H}_3(\omega,\omega,3\omega) = [\mathcal{H}_1(\omega)]^2\mathcal{H}_1(3\omega)\mathcal{H}_1(5\omega)\left\{\frac{2\varrho^2[2\mathcal{H}_1(4\omega)+\mathcal{H}_1(2\omega)]}{3}-\lambda_3\right\}, \tag{59}$$

$$\mathcal{H}_3(\omega,3\omega,3\omega) = \mathcal{H}_1(\omega)[\mathcal{H}_1(3\omega)]^2\mathcal{H}_1(7\omega)\left\{\frac{2\varrho^2[2\mathcal{H}_1(4\omega)+\mathcal{H}_1(6\omega)]}{3}-\lambda_3\right\} \tag{60}$$

All the kernels described by Eqs. (57)–(60) show that the term $\varrho^2$ is always greater than zero, which indicates that the third-order kernels are independent of the regime cycles and maintains the same framework. Moreover, the presence of sub-harmonics in the third-order kernels is more pronounced. For instance, the cross-kernel $\mathcal{H}_3(\omega,3\omega,3\omega)$ shows sub-harmonics at frequencies $3\omega, 4\omega, 6\omega$ and $7\omega$. This analysis is simple to carry out when the leading diagonal is known.

### 3.2. Total response in time domain

The output response of the system with hysteresis (33) described analytically by the Volterra series up to third-order contributions is given by:

$$y(t) = y_1(t) + y_2(t) + y_3(t) \tag{61}$$

splitting the second-order contribution according to the loading–unloading cycles:

$$y_2(t) = \frac{1+\Phi[\dot{u}(t)]}{2}y_2^{\uparrow}(t) + \frac{1-\Phi[\dot{u}(t)]}{2}y_2^{\downarrow}(t) \tag{62}$$

where $\Phi[\dot{u}(t)]$ is used to ensure a smooth transition between each load regime. Thus, the polynomial contributions of the total response $y(t)$ described by Volterra series are calculated considering the following input:

$$\begin{aligned}&u(t) = \tfrac{A\left(e^{j\omega t}+e^{-j\omega t}\right)}{2}, \\ &u(t) = A_1\left(e^{j\omega t}+e^{-j\omega t}\right) + A_2\left(e^{j3\omega t}+e^{-j3\omega t}\right)\end{aligned} \tag{63}$$

the contributions are given by:

$$y_1(t) = \frac{A}{2}\mathcal{H}_1(\omega)e^{j\omega t} + A_1\mathcal{H}_1(\omega)e^{j\omega t} + A_2\mathcal{H}_1(3\omega)e^{j3\omega t} + \text{complex conjugates} \tag{64}$$

$$\begin{aligned} y_2^{\uparrow}(t) = {} & \tfrac{A^2}{2}\mathcal{H}_2(\omega,-\omega) - 2A_1^2\mathcal{H}_2(\omega,-\omega) - 2A_2^2\mathcal{H}_2(3\omega,-3\omega) + \\ & \tfrac{A^2}{4}\mathcal{H}_2(\omega,\omega)e^{j2\omega t} + A_1^2\mathcal{H}_2(\omega,\omega)e^{j2\omega t} + A_2^2\mathcal{H}_2(3\omega,3\omega)e^{j6\omega t} + \\ & AA_1\mathcal{H}_2(\omega,\omega)e^{j2\omega t} + AA_2\mathcal{H}_2(-\omega,3\omega)e^{j2\omega t} + AA_2\mathcal{H}_2(\omega,3\omega)e^{j4\omega t} - \\ & A_1A_2\mathcal{H}_2(-\omega,3\omega)e^{j2\omega t} + A_1A_2\mathcal{H}_2(\omega,3\omega)e^{j4\omega t} + \text{complex conjugates} \end{aligned} \tag{65}$$

$$y_2^{\downarrow}(t) = -y_2^{\uparrow}(t) \tag{66}$$

$$\begin{aligned} y_3(t) = {} & \tfrac{3A^3}{8}\mathcal{H}_3(\omega,\omega,-\omega)e^{j\omega t} - 3A_1^3\mathcal{H}_3(\omega,\omega,-\omega)e^{j\omega t} + \\ & \tfrac{3A^2A_1}{4}\mathcal{H}_3(\omega,\omega,-\omega)e^{j\omega t} + \tfrac{3A^2A_2}{4}\mathcal{H}_3(-\omega,-\omega,3\omega)e^{j\omega t} - \\ & \tfrac{3AA_1^2}{2}\mathcal{H}_3(-\omega,-\omega,3\omega)e^{j\omega t} - 3AA_2^2\mathcal{H}_3(\omega,-3\omega,3\omega)e^{j\omega t} + \\ & 3A_1^2A_2\mathcal{H}_3(-\omega,-\omega,3\omega)e^{j\omega t} - 6A_1A_2^2\mathcal{H}_3(\omega,-3\omega,-3\omega)e^{j\omega t} + \\ & \tfrac{A^3}{8}\mathcal{H}_3(\omega,\omega,\omega)e^{j3\omega t} + A_1^3\mathcal{H}_3(\omega,\omega,\omega)e^{j3\omega t} - \\ & 3A_2^3\mathcal{H}_3(3\omega,3\omega,-3\omega)e^{j3\omega t} + \tfrac{3A^2A_1}{4}\mathcal{H}_3(\omega,\omega,\omega)e^{j3\omega t} + \\ & \tfrac{3A^2A_2}{2}\mathcal{H}_3(-\omega,\omega,3\omega)e^{j3\omega t} + \tfrac{3AA_1^2}{2}\mathcal{H}_3(\omega,\omega,\omega)e^{j3\omega t} - \\ & 6A_1^2A_2\mathcal{H}_3(\omega,-\omega,3\omega)e^{j3\omega t} + \tfrac{3A^2A_2}{4}\mathcal{H}_3(\omega,\omega,3\omega)e^{j5\omega t} + \\ & \tfrac{3AA_2^2}{2}\mathcal{H}_3(-\omega,3\omega,3\omega)e^{j5\omega t} + 3A_1^2A_2\mathcal{H}_3(\omega,\omega,3\omega)e^{j5\omega t} - \\ & 3A_1A_2^2\mathcal{H}_3(-\omega,3\omega,3\omega)e^{j5\omega t} + \tfrac{3AA_2^2}{2}\mathcal{H}_3(\omega,3\omega,3\omega)e^{j7\omega t} + \\ & 3A_1A_2^2\mathcal{H}_3(\omega,3\omega,3\omega)e^{j7\omega t} + A_2^3\mathcal{H}_3(3\omega,3\omega,3\omega)e^{j9\omega t} \\ + {} & \text{complex conjugates} \end{aligned} \tag{67}$$

**Remark 3.1.** Although the harmonics present in the contributions $y_2^{\uparrow}(t)$ and $y_2^{\downarrow}(t)$ are from even order such as $e^0, e^{2\omega t}, e^{4\omega t}$ and $e^{6\omega t}$, the multiplication in Eq. (62) by $\Phi[\dot{u}(t)]$ causes odd harmonics $e^{\omega t}, e^{3\omega t}, e^{5\omega t}$, and so on, to appear. Hence, the harmonic of higher order generated by $y_2(t)$ must also be in $y_3(t)$, otherwise, the odd harmonics generated does not match those in the response of the oscillator. To meet this condition, the number of terms $N_s$ to approximate $\Phi[\dot{u}(t)]$ needs to be the same as the one used to compute the input $u_0(t)$.

The main advantage in estimating the higher-order FRFs is the dependence that they have on the physical parameters of the system and its linear FRF. Another interesting aspect is that the Volterra kernels provide an approximate overview in frequency domain about the nonlinear behavior occurring in the oscillator with hysteresis for the applied input condition. Thus, as long as the higher-order FRFs and the Volterra series are convergent, the outputs in the time and frequency domain provide a unique mapping from the system dynamics, a characteristic that the short-time Fourier transform has for non-stationary signals.

## 4. Numerical application

With the analytical higher-order FRFs derived from the system composed of the nonlinear operator, this section aims to explore the applicability of these expressions to describe a hysteretic benchmark with a dynamic nonlinearity well approximated by a Bouc-Wen model and recently proposed by Noël and Shoukens (2016) [29] at the Workshop on Nonlinear System Identification Benchmarks. Although the white-box methods have improved their applicability to complex nonlinear systems, the main contributions in the literature for the Bouc-Wen model or even for the proposed benchmark are with gray-box and black-box approaches. For instance, Noël et al. (2017) [53] used a framework based on black-box identification to deal with the hysteresis effect without the requirement of a specific physical model. The algorithm procedure consists of identifying polynomial nonlinear state-space (PNLSS) models fitted under multisine excitation. Then, to reduce the high number of terms required to identify the PLNSS model, Esfahani et al. (2018) [30] proposed using the canonical polyadic decomposition, which rewrites the univariate polynomials in linear combinations of states and inputs.

From the perspective of grey-box modeling, Worden et al. (2018) [33] provided an identification scheme to obtain the Bouc-Wen model parameters based on an evolutionary optimization algorithm. The procedure has also addressed issues about the adequate choice of excitation inputs and reference models. In addition, Bajrić and Høgsberg (2018) [31] used stochastic output-only subspace methods to identify the poles of an equivalent linear damper model parametrized according to the excitation amplitude, frequencies, and benchmark model parameters. Furthermore, the work provides interesting physical insight about the benchmark behavior under different forcing conditions, since the equivalences considered to

construct the linear system were based on intrinsic characteristics from slow and fast motion regimes of the Bouc-Wen oscillator.

The Bouc-Wen benchmark model parameters are shown in Table 1 and were selected according to [29]. First, this section starts with a numerical example of the nonlinear operator shown in the motion Eq. (17) to describe a hysteretic system. Thus, through the higher-order FRFs framework applied to the nonlinear operator, the analytical output from the system with hysteresis is calculated and compared to the output obtained by the numerical integration with 4$^{th}$ order Runge–Kutta method. The Volterra contributions and the higher-order kernel surfaces are also provided.

### 4.1. Numerical example of the nonlinear operator

Some numerical simulations are carried out to evaluate the nonlinear operator proposed to describe hysteretic systems. All simulations with the benchmark presented in this work used a sampling frequency equal to 750 Hz and $N = 2^{14}$ samples with the parameters listed in Table 1. The numerical integration was solved through the 4$^{th}$ order Runge–Kutta method with a variable time step. A convergence analysis based on the terms selected to be used in the Taylor series expansion considering a varying number of terms from the Fourier series is carried out to illustrate that the framework of the nonlinear operator, defined in Eq. (17), is suitable to deal with the Bouc-Wen benchmark. The error is calculated by the Normalized Mean Square Error (NMSE) [%] between the responses from the Bouc-Wen oscillator and from the system in (17):

$$\text{NMSE} = 100 \times \frac{\left\| \mathcal{Z}(y,\dot{y}) - \mathcal{F}[y(t)] \right\|_2}{\left\| \mathcal{Z}(y,\dot{y}) \right\|_2} \% \tag{68}$$

Fig. 2 depicts four different cases of the NMSE in function of the excitation amplitudes considering a quasi-static harmonic input $u(t) = A\cos(2\pi t)$. Regardless of the number of terms used in the Fourier series are used, the NMSE in Fig. 2(a) indicates that the nonlinear operator fails to describe the hysteretic restoring force when it assumes less than three terms in the Taylor series expansion. For expansions from the 3rd order on, Figs. 2(b)-(d) show that the nonlinear operator reaches the convergence, with values below of 2.5%, if $N_s \geqslant 2$. In conclusion, since the framework of the nonlinear operator provides an interesting cost-effective ratio between accuracy and algebraic complexity of the higher-order FRFs, the third-order polynomial form in the bounding functions with $N_s = 2$ is adequate to describe and reproduce the benchmark hysteresis loop.

Fig. 3 shows the simulated response of the Bouc-Wen model described in Section 2.2 considering a quasi-static harmonic input with amplitude of $A = 120$ N selected based on [29]. Under this excitation condition, the model with RIH property draws a single hysteresis loop bounded between loading and unloading regions. The restoring force obtained through numerical integration of the Eqs. (4) and (5) is plotted in Fig. 3(a) by considering null initial conditions. Fig. 3(b) shows the restoring force $\times$ displacement graphic, where it is possible to clearly note that the continuous hysteresis loop is bounded over the output amplitudes $[-Y, Y]$ and the symmetric loading and unloading regimes of the restoring force.

The displacement amplitudes $Y$ and $y_0$ obtained are 0.9502 mm and 0.2536 mm, respectively. These two amplitudes were used to compute the bounding functions coefficients through the Eqs. (20)–(23). The absolute values obtained are $\lambda_0 = 13.88$ N, $\lambda_1 = 5 \times 10^4$ N/m, $\lambda_2 = 1.0941 \times 10^7$ N/m$^2$ and $\lambda_3 = 3.0665 \times 10^{10}$ N/m$^3$. By solving numerically the motion Eq. (17), the equivalent restoring force from the nonlinear operator is able to reproduce the force $\mathcal{Z}(y,\dot{y})$ properly, as can been seen in Fig. 3(a). Furthermore, the enclosed area of the hysteresis loops depicted in Fig. 3(b) is almost the same for both restoring forces, which means that these systems have the same energy dissipation [Nmm].

### 4.2. The Bouc-Wen benchmark

A harmonic quasi-static input $u(t) = A\cos(2\pi t)$ with amplitude of $A = 40$ N was used and the system outputs were obtained through numerical integration of the motion Eqs. (4) and (5) based on the 4th order Runge-Kutta method. For quasi-static input conditions, the selected amplitude $A = 40$ N reproduces a weak hysteresis loop. Amplitudes of $Y = 0.3641$ mm and $y_0 = 0.0445$ mm were obtained to compute the coefficients $\lambda_0, \lambda_1, \lambda_2$ and $\lambda_3$ used in the higher-order FRFs.

The parameters $m, c, k$ and $\alpha$ from Table 1 were used to calculate the kernels $\mathcal{H}_1(\omega)$ and $\mathcal{H}_1(3\omega)$ over a frequency range of $0 - 71.30$ Hz with an incremental step of 0.046 Hz. Fig. 4 shows the first order FRF both in terms of its magnitude (Fig. 4) and phase (Fig. 4(b)). The resonance peaks are 35.58 and $\frac{35.6}{3}$ Hz, which means that the resonances occur at $\omega_n$, which is

**Table 1**
Bouc-Wen benchmark parameters [29].

| $m$ [kg] | $c$ [Ns/m] | $k$ [N/m] | $\alpha$ [N/m] | $\beta$ | $\gamma$ [m$^{-1}$] | $\delta$ [m$^{-1}$] | $\nu$ |
|---|---|---|---|---|---|---|---|
| 2 | 10 | $5 \times 10^4$ | $5 \times 10^4$ | $1 \times 10^3$ | 0.8 | −1.1 | 1 |

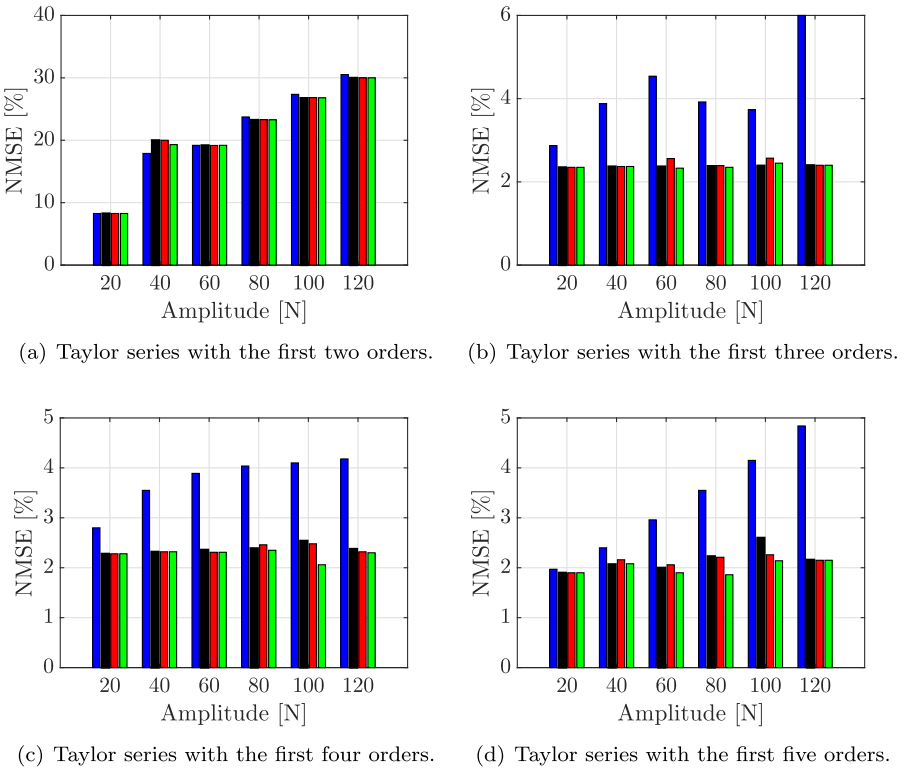


(a) Taylor series with the first two orders. (b) Taylor series with the first three orders.

(c) Taylor series with the first four orders. (d) Taylor series with the first five orders.

**Fig. 2.** Convergence analysis of the nonlinear operator representing the hysteretic restoring force of the Bouc-Wen benchmark. ■ represents $N_s = 1$, ■ represents $N_s = 2$, ■ represents $N_s = 3$ and ■ is for $N_s = 4$.

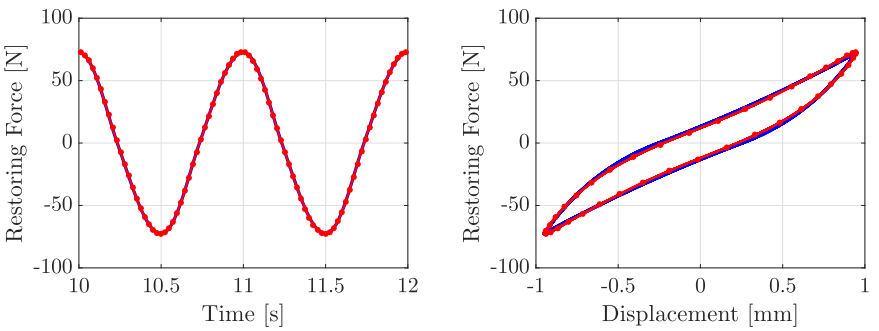


(a) Restoring force response. (b) Hysteresis loop.

**Fig. 3.** Comparison between the restoring forces obtained from the Bouc-Wen oscillator and through the nonlinear operator. – – – for the Bouc-Wen's response and – • – is for the nonlinear operator. The NMSE obtained is 2.15% and the dissipated energy of both hysteretic loops is ≈ 42.35 N mm.

associated with the linear dynamic of the model, and at $3\omega = \omega_n \Rightarrow \omega = \frac{\omega_n}{3}$, associated with the third order harmonic from the additional input.

In the case of an equivalent system that does not hold the principle of superposition, its response presents the frequency components from the input as well as multiple harmonics from the nonlinear behavior. The interactions between the frequency components that the system presents are clear in the second and third order FRFs equations, with components of $5\omega, 6\omega$ and $7\omega$ order, among others. Thus, Figs. 5 and 7 show the magnitude and phase surface of each kernel, whereas Figs. 6 and 8 are their leading diagonal.

Figs. 5(a) and (b) present the surfaces from $\mathcal{H}_2(\omega_1, \omega_2)$ on the components $\omega_1$ and $\omega_2$, whereas Figs. 6(a) and (b) show the leading diagonal in $\omega_1 = \omega_2 = \omega$, where $f_1 = \frac{\omega_1}{2\pi}$ and $f_2 = \frac{\omega_2}{2\pi}$. These plots evidence the resonance peaks at 35.58 and 17.79 Hz ($2\omega = \omega_n$), which refer to the linear and secondary resonances. Although the total output does not have quadratic components, the FRF framework provides knowledge about the bounding functions nonlinearity. Furthermore, the changes in $\lambda_2$

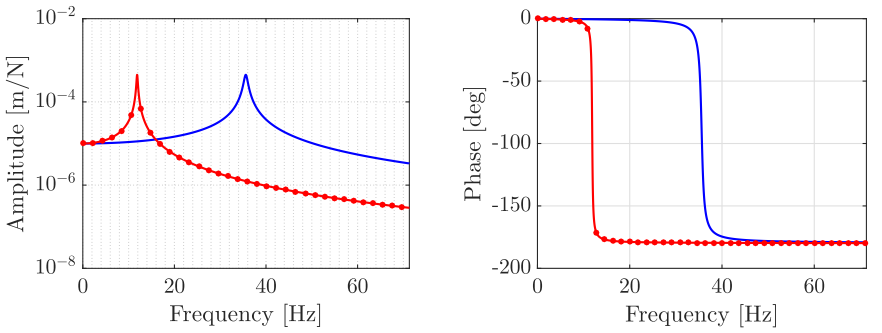


(a) Amplitude. (b) Phase.

**Fig. 4.** Frequency Response Functions. – represents the kernel $\mathcal{H}_1(\omega)$, whereas – • – is for the kernel $\mathcal{H}_1(3\omega)$.

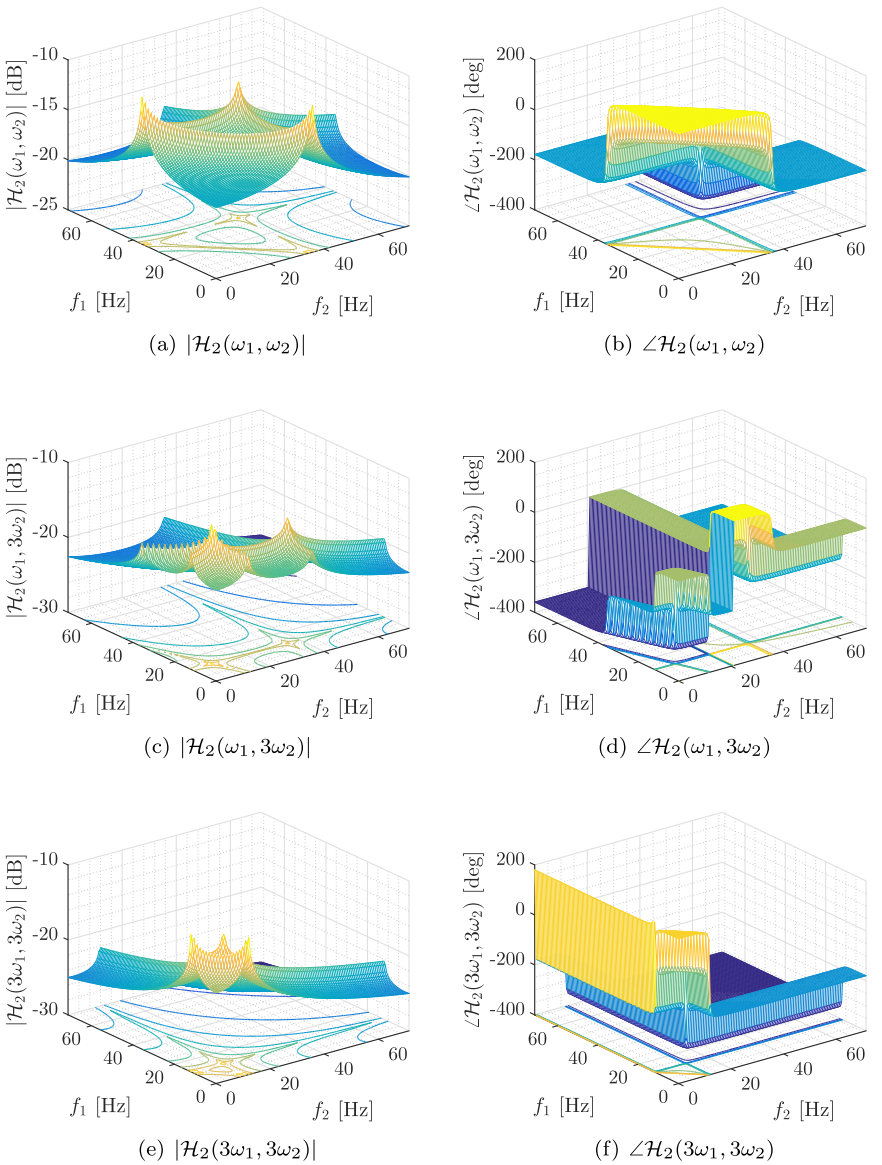


(a) $|\mathcal{H}_2(\omega_1,\omega_2)|$ (b) $\angle\mathcal{H}_2(\omega_1,\omega_2)$

(c) $|\mathcal{H}_2(\omega_1,3\omega_2)|$ (d) $\angle\mathcal{H}_2(\omega_1,3\omega_2)$

(e) $|\mathcal{H}_2(3\omega_1,3\omega_2)|$ (f) $\angle\mathcal{H}_2(3\omega_1,3\omega_2)$

**Fig. 5.** Second-order Volterra kernels.

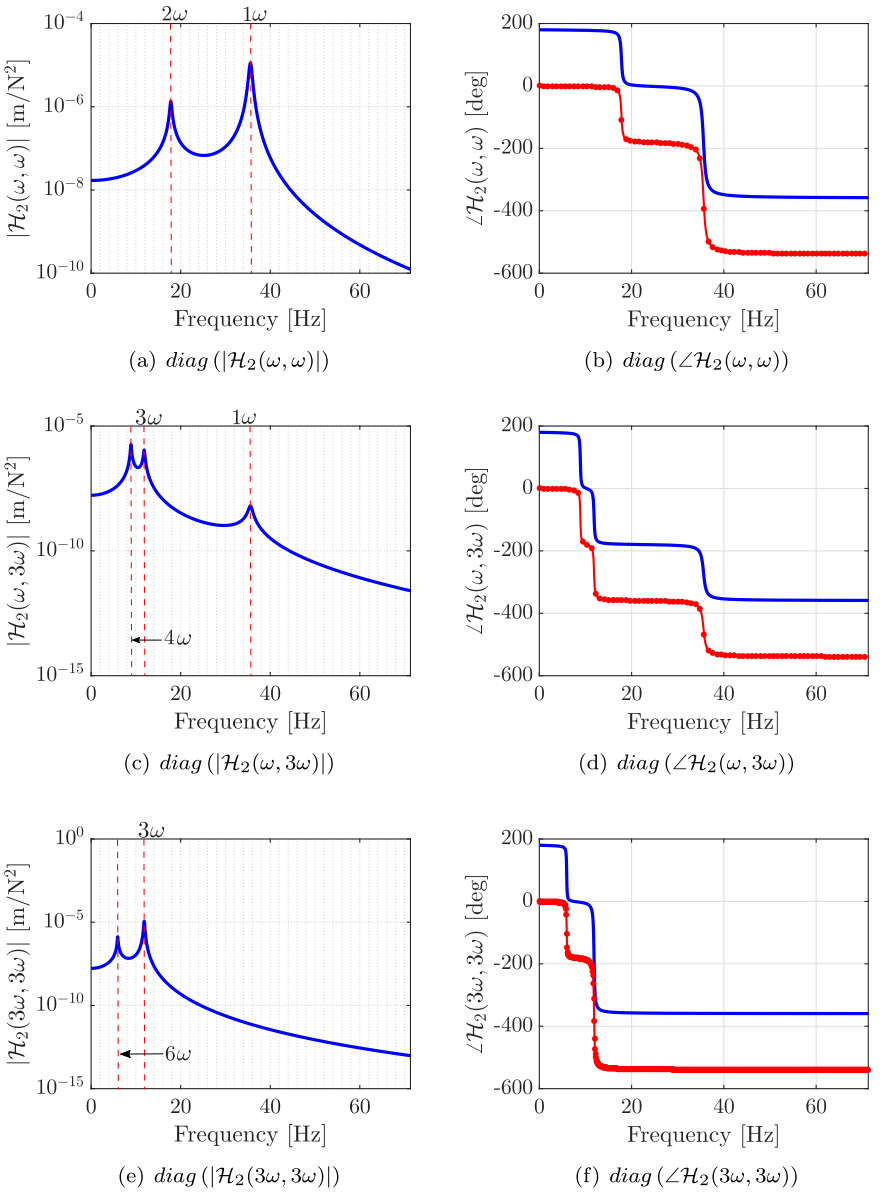


**Fig. 6.** Leading diagonals of the second-order Volterra kernels. – represents the kernels with $\lambda_2 > 0$, whereas – • – is for the kernels that have $\lambda_2 < 0$.

influence on the phase plot, as shown in Fig. 6, whereas the surfaces depicted in Fig. 5 exemplify only the second order FRFs that have $\lambda_2 > 0$.

Figs. 5(c) and (d) illustrate the second-order cross-kernel surfaces that highlight the interaction between frequency components with the inputs. Additionally, Figs. 6(c)-(d) show the amplitude and phase of the leading diagonals, thus evidencing the main resonance at 35.58 and the secondary resonances at 11.86 and 8.89 Hz, corresponding to the harmonics of $3\omega = \omega_n$ and $4\omega = \omega_n$, respectively. Finally, the plot of surfaces in Figs. 5(e) and (f) with their leading diagonals in Fig. 6(e) and (f) shows the direct kernel calculated with the additional input evidencing the resonance peaks at 11.86 and 5.93 Hz ($6\omega = \omega_n$), which is an interaction that the third-order harmonic input holds in the second order kernel.

The framework of the third-order kernels plotted in Fig. 7 shows surfaces on the frequency components $\omega_1, \omega_2$ and sliced at $\omega_3 = \frac{\omega_n}{3}$. Visualizing the presence of sub-harmonics and resonance peaks, as well as phase jumps in these surfaces, is not trivial and it needs the support of each leading diagonal, which is plotted in Fig. 8. All the third-order kernels have in their leading diagonal, depicted as amplitude and phase plots, weak resonances in secondary sub-harmonics, indicating the influence that quadratic nonlinearities have on these kernels. Nevertheless, the peaks with major amplitude are regarded as tertiary sub-harmonics, which highlight the domain of cubic nonlinearity over the frequency response. Although the calculation

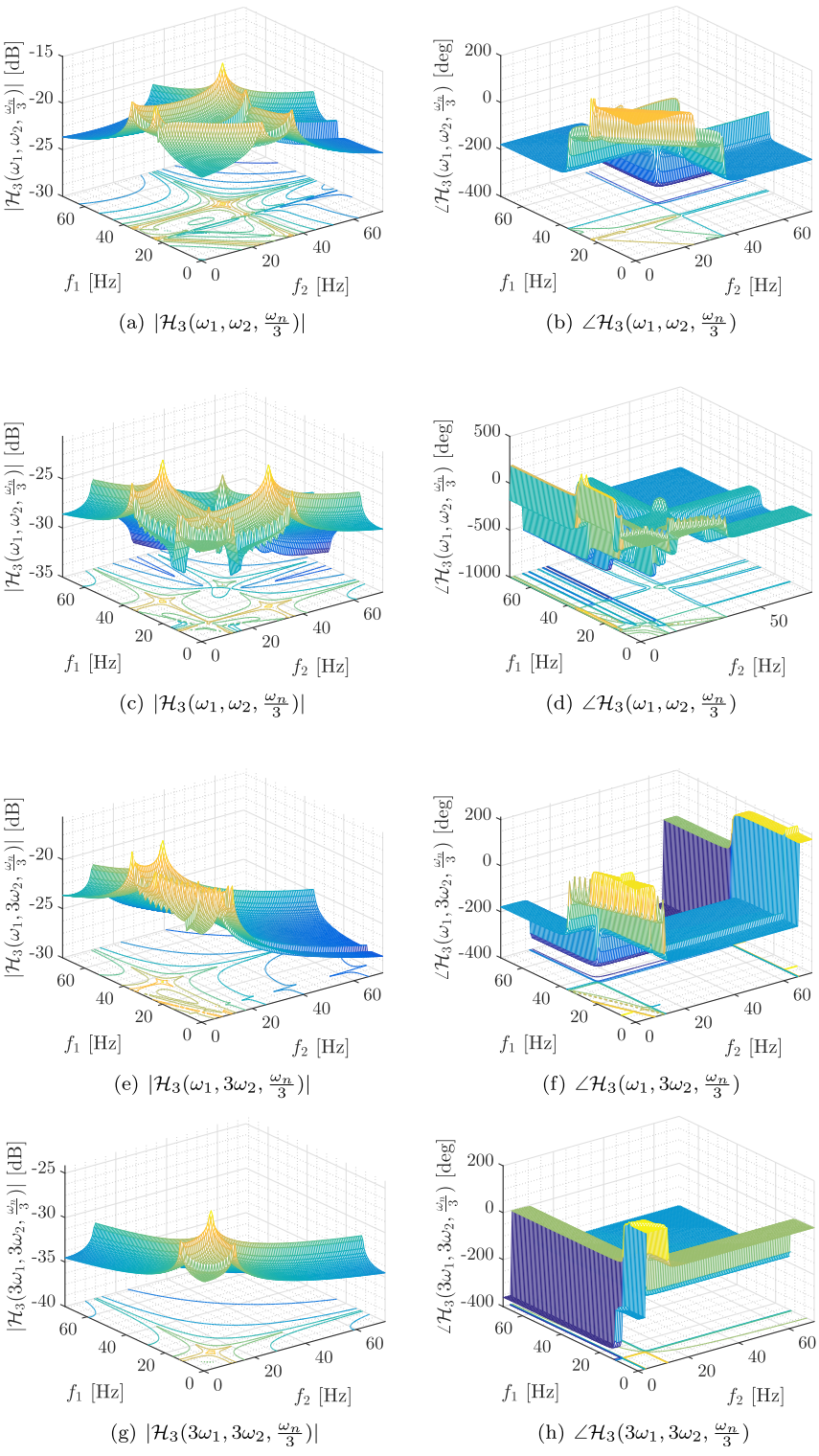


(a) $|\mathcal{H}_3(\omega_1,\omega_2,\frac{\omega_n}{3})|$ (b) $\angle\mathcal{H}_3(\omega_1,\omega_2,\frac{\omega_n}{3})$

(c) $|\mathcal{H}_3(\omega_1,\omega_2,\frac{\omega_n}{3})|$ (d) $\angle\mathcal{H}_3(\omega_1,\omega_2,\frac{\omega_n}{3})$

(e) $|\mathcal{H}_3(\omega_1,3\omega_2,\frac{\omega_n}{3})|$ (f) $\angle\mathcal{H}_3(\omega_1,3\omega_2,\frac{\omega_n}{3})$

(g) $|\mathcal{H}_3(3\omega_1,3\omega_2,\frac{\omega_n}{3})|$ (h) $\angle\mathcal{H}_3(3\omega_1,3\omega_2,\frac{\omega_n}{3})$

**Fig. 7.** Third-order Volterra kernels.

of kernels was carried out for a specific input condition, their framework in the frequency domain will remain the same for other conditions, experiencing changes only with respect to their amplitudes, since the first-order kernels still maintain same values due to the linear physical parameters.

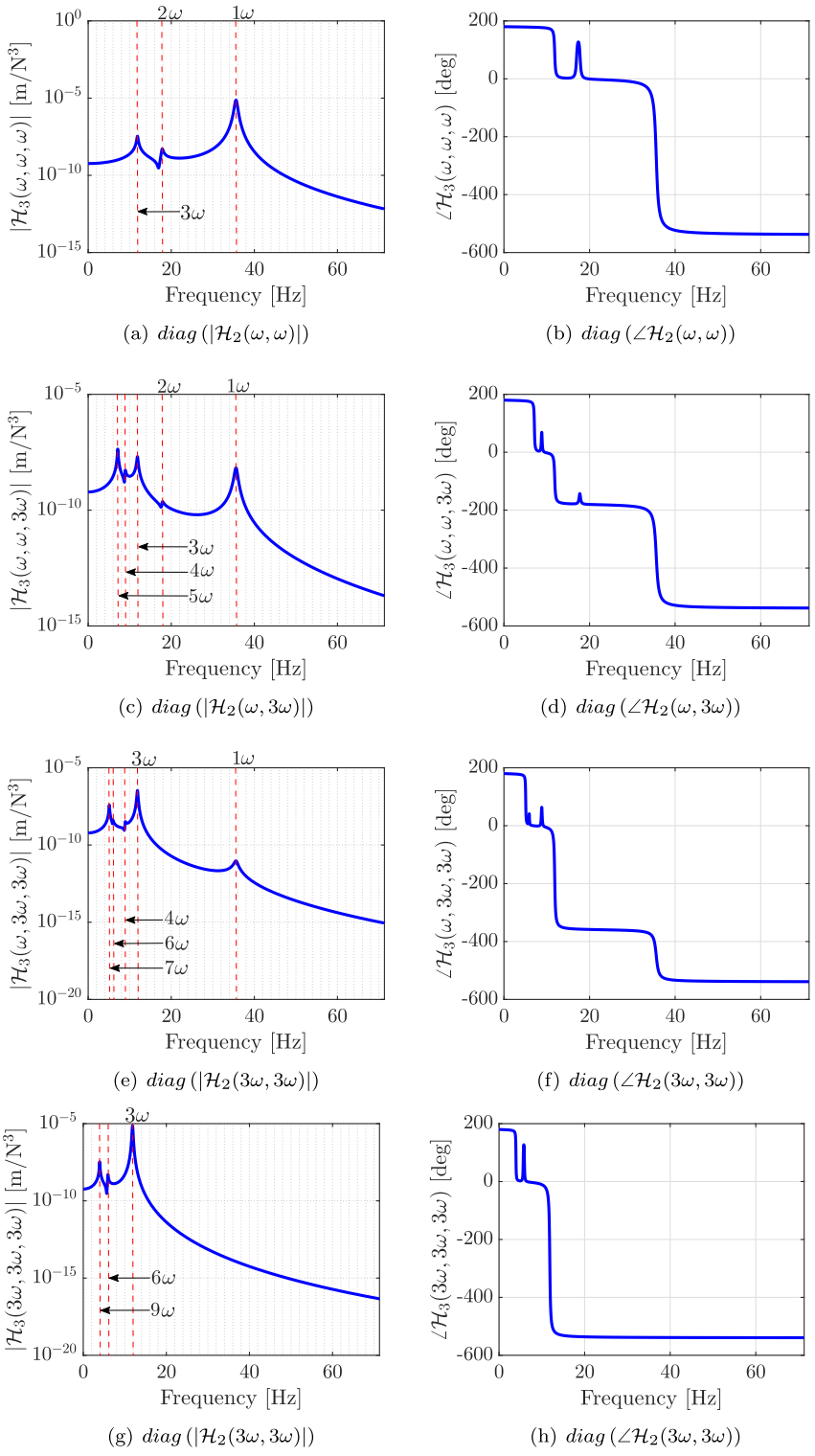


**Fig. 8.** Leading diagonals of the third-order Volterra kernels.

Having the higher-order FRFs, the analytical polynomial contributions $y_1(t), y_2(t)$ and $y_3(t)$ are estimated in time domain through the Eqs. (64)–(67) with frequency $\omega = 2\pi$. Fig. 9 presents a comparison between the output generated by numerical integration and the analytical one, which demonstrates a good match between the results. Fig. 10 shows a close-up view of

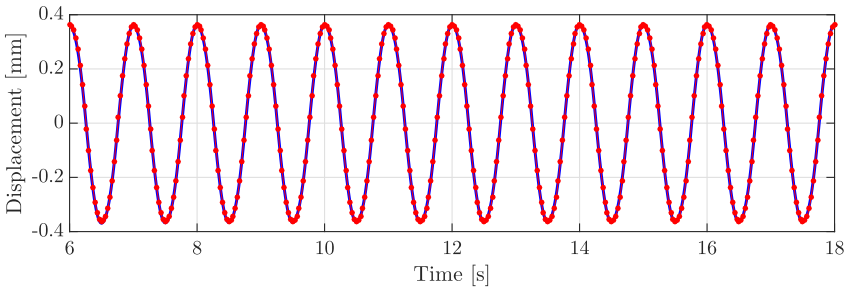


**Fig. 9.** Output of the identified Volterra model in a close-up view over 6 – 18 seconds. – represents the response of the Bouc-Wen oscillator by numerical integration and • is the response of the proposed Volterra model. The value of NMSE computed between the outputs is 2.7%.

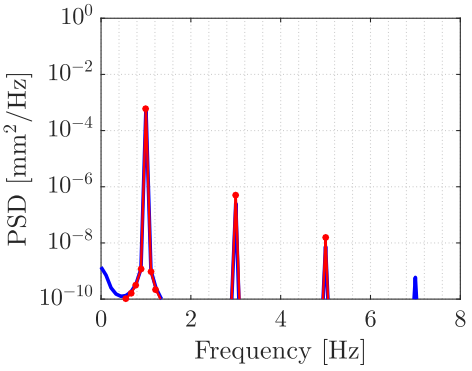


**Fig. 10.** Comparison between the outputs spectrum. – represents the output spectrum simulated from the Bouc-Wen and • is the spectrum predicted by the proposed Volterra model.

the response spectrum over a frequency range of 0 – 8 Hz, evidencing the excitation frequency at 1 Hz and also the third, fifth and seventh-order harmonics at 3, 5 and 7 Hz, respectively. Welch's periodogram with a rectangular window over a frequency range of 0 – 70 Hz was used to attain this. The Volterra model can reproduce up to the fifth-order harmonic component (5 Hz), but more terms in the series expansion are necessary to predict higher-order components. However, the number of terms included in this work is sufficient to deal with the Bouc-Wen model subjected to weak excitation inputs.

The nonlinear contributions $y_2(t) + y_3(t)$ oscillate with a phase shift in comparison with the linear contribution, which highlight the nonlinear damping that arises from the hysteresis effect. Even with the presence of the second-order contribution $y_2(t)$, the total response of the Volterra model has only odd harmonics, as discussed in Remark 3.1. In addition, Fig. 11 depicts the linear and nonlinear contributions of the total response in time domain (Fig. 11) and each output spectrum (Fig. 11(b)), which is a demonstration of Remark 3.1, since the second-order contribution has components at 1, 3 and 5 Hz, as well as the third-order contribution. With the influence of the additional input, the linear output $y_1(t)$ has components at 1 and 3 Hz.

The odd harmonics presented in the response spectrum are not enough to conclude if the analytical output describes well the hysteresis loop since other nonlinearities could show the same behavior [54]. Fig. 12 shows the comparison between the

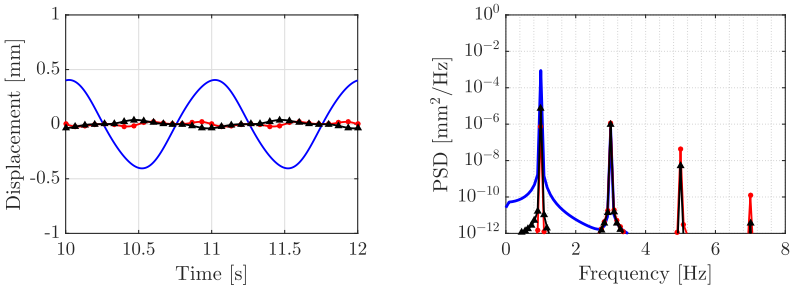


(a) Contributions. (b) Outputs spectrum

**Fig. 11.** Representation of the Volterra model contributions. –, $y_1(t)$; – • –, $y_2(t)$ and –▲–, $y_3(t)$.

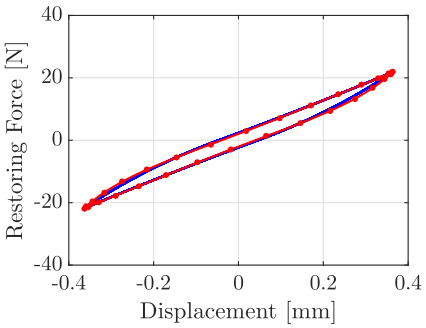


**Fig. 12.** Comparison between the hysteresis loop responses with excitation amplitude of $A = 40$ N. – represents the restoring force of the Bouc-Wen model and • is the restoring force estimated through the Volterra model output.

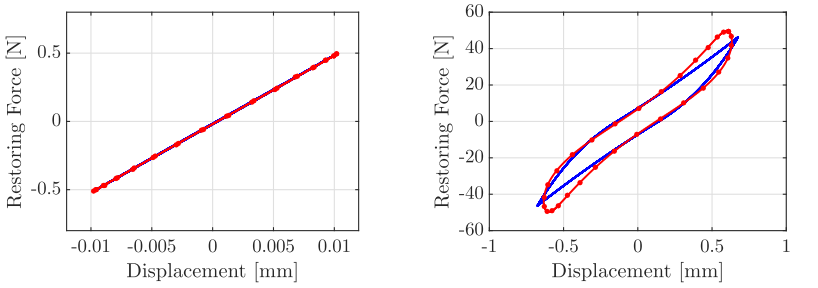


(a) Low amplitude level of $A = 1$ N. (b) High amplitude level of $A = 60$ N.

**Fig. 13.** Bouc-Wen hysteresis loop for different forcing amplitudes. – represents the restoring force calculated through numerical integration and • is the restoring force by the Volterra model output.

smoothed hysteresis loop obtained with the Volterra model and by numerical integration, whose loops dissipate 2.61% Nmm and 2.5% Nmm respectively, demonstrating that the analytical response is able to reproduce with a reasonable agreement the Bouc-Wen oscillator hysteresis loop.

Fig. 13 illustrates the hysteresis loop obtained through the Volterra model for different forcing amplitudes and the same excitation frequency. In the case of low amplitude with $A = 1$ N, as plotted in Fig. 13(a), the analytical output can reproduce the hysteresis loop with a good match, which is almost closed and the restoring force is linear. However, when the input amplitude gets higher, as seen in Fig. 13(b) with $A = 60$ N, the Volterra model starts presenting convergence problems, for instance, the dissipated energy by the analytical model is 4.52 Nmm, whereas the value of 3.75 Nmm is obtained from the numerical integration. In fact, although the mathematical framework helps overcome difficulties to represent discontinuities and multiple solutions on the hysteresis loop, the Volterra series is adequate to describe hysteretic systems under

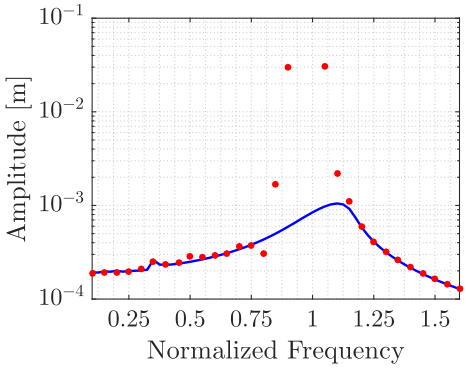


**Fig. 14.** Comparison between the response amplitudes for a sweep sine input. – represents the numerical response from the Bouc-Wen and • is the spectrum predicted by the proposed Volterra model.

weak excitation amplitudes and conditions where the hysteresis loop is almost closed. The methodology presented in this work can be an alternative tool of an algorithm to perform a modal analysis on a hysteretic system.

Finally, Fig. 14 shows the comparison between the response amplitudes estimated through numerical integration and by Volterra model for a sweep sine test with constant input amplitude of $A = 20$ N over a normalized frequency range $\frac{\omega}{\omega_n} \in [0.1 \quad 1.6]$. The proposed smooth nonlinear operator has quadratic terms that are taken into account to compute the second-order kernels and, for this reason, the amplitude of the second-order contributions increase when $\frac{\omega}{\omega_n} = 0.5$, whereas the Bouc-Wen output does not present this sub-harmonic. In addition, around the linear resonance frequency range $\frac{\omega}{\omega_n} \in [0.75 \quad 1.2]$, the analytical Volterra model is absolutely inaccurate. The result clearly details that the response predicted by the Volterra model is only suitable for a narrow-banded input conditions.

## 5. Final remarks

This work presents the use of the Volterra series to represent hysteretic systems based on the analytical higher-order FRFs estimated through the harmonic probing method. Initially, the existence of bounding functions was discussed by the polynomial form to approximate independently each loading regime that occurs along the hysteresis loop. The combination of these functions into an equivalent system allowed the application of the harmonic probing method for multi-input systems, and to derive expressions for the higher-order FRFs. The proposed methodology includes the hysteresis memory effect in the output predicted through the Volterra model by considering an additional input that depends on the input signal rate of change and guarantees multiple solutions to the analytical higher-order FRFs. The effectiveness of the proposed solution was tested using a benchmark involving the Bouc-Wen model. The results obtained show that for narrow-banded input conditions with weak excitation amplitudes, the Volterra series can provide an adequate analytical approximation. With representation proposed using Volterra kernels, it is possible to identify all the parameters from the higher-order FRFs using experimental data in future works.

## Acknowledgments

The authors are thankful for the financial support provided by São Paulo Research Foundation (FAPESP) Grant No. 2016/21973-5 and 2017/15512-8 and CNPq Grant No. 307520/2016-1. Additionally, the authors would like to thank the anonymous reviewers and the Associate Editor for their relevant comments and useful suggestions.

## References

[1] A. Visintin, Differential Models of Hysteresis, 111, Springer Science & Business Media, 2013.
[2] B.F. Spencer, S.J. Dyke, M.K. Sain, J.D. Carlson, Phenomenological model of a magnetorheological dampers, J. Eng. Mech. 123 (3) (1996) 230–238.
[3] S.J. Dyke, B.F.S. Jr, M.K. Sain, J.D. Carlson, An experimental study of MR dampers for seismic protection, Smart Mater. Struct. 7 (5) (1998) 693, URLhttp://stacks.iop.org/0964-1726/7/i=5/a=012.
[4] Y. Peng, J. Yang, J. Li, Parameter identification of modified Bouc-Wen model and analysis of size effect of magnetorheological dampers, J. Intell. Mater. Syst. Struct. 29 (7) (2017) 1464–1480, https://doi.org/10.1177/1045389X17740963, arXiv: https://doi.org/10.1177/1045389X17740963.
[5] A. Dominguez, R. Sedaghati, I. Stiharu, Modeling and application of MR dampers in semi-adaptive structures, Comput. Struct. 86 (3) (2008) 407–415, https://doi.org/10.1016/j.compstruc.2007.02.010, Smart Structures.http://www.sciencedirect.com/science/article/pii/S004579490700082X..
[6] H. Ahmadian, H. Jalali, Generic element formulation for modelling bolted lap joints, Mech. Syst. Signal Process. 21 (5) (2007) 2318–2334, https://doi.org/10.1016/j.ymssp.2006.10.006, URLhttp://www.sciencedirect.com/science/article/pii/S0888327006002263.
[7] H. Ahmadian, H. Jalali, F. Pourahmadian, Nonlinear model identification of a frictional contact support, Mech. Syst. Signal Process. 24 (8) (2010) 2844–2854, https://doi.org/10.1016/j.ymssp.2010.06.007, URLhttp://www.sciencedirect.com/science/article/pii/S0888327010001998.
[8] F. Pourahmadian, H. Ahmadian, H. Jalali, Modeling and identification of frictional forces at a contact interface experiencing micro-vibro-impacts, J. Sound Vib. 331 (12) (2012) 2874–2886, https://doi.org/10.1016/j.jsv.2012.01.032, URLhttp://www.sciencedirect.com/science/article/pii/S0022460X12001022.
[9] F. Ikhouane, J. Rodellar, Systems with Hysteresis: Analysis, Identification and Control Using the Bouc-Wen Model, John Wiley & Sons, 2007.
[10] V. Hassani, T. Tjahjowidodo, T.N. Do, A survey on hysteresis modeling, identification and control, Mech. Syst. Signal Process. 49 (1) (2014) 209–233, https://doi.org/10.1016/j.ymssp.2014.04.012, ULRhttp://www.sciencedirect.com/science/article/pii/S0888327014001186.
[11] R. Bouc, A mathematical model for hysteresis, Acta Acustica united with Acustica 24 (1) (1971) 16–25, URLhttp://www.ingentaconnect.com/content/dav/aaua/1971/00000024/00000001/art00004.
[12] Y.-K. Wen, Method for random vibration of hysteretic systems, J. Eng. Mech. Div. 102 (2) (1976) 249–263.
[13] N. Okuizumi, K. Kimura, Multiple time scale analysis of hysteretic systems subjected to harmonic excitation, J. Sound Vib. 272 (3) (2004) 675–701, https://doi.org/10.1016/S0022-460X(03)00404-8, URLhttp://www.sciencedirect.com/science/article/pii/S0022460X03004048.
[14] F. Ikhouane, J. Rodellar, On the hysteretic Bouc-Wen model, Nonlinear Dyn. 42 (1) (2005) 79–95, https://doi.org/10.1007/s11071-005-0070-x.
[15] Y. Shen, M.F. Golnaraghi, G.R. Heppler, Analytical and experimental study of the response of a suspension system with a magnetorheological damper, J. Intell. Mater. Syst. Struct. 16 (2) (2005) 135–147, https://doi.org/10.1177/1045389X05048330, arXiv: https://doi.org/10.1177/1045389X05048330.
[16] H. Jalali, An alternative linearization approach applicable to hysteretic systems, Commun. Nonlinear Sci. Numer. Simul. 19 (1) (2014) 245–257, https://doi.org/10.1016/j.cnsns.2013.05.020, URLhttp://www.sciencedirect.com/science/article/pii/S1007570413002220.
[17] S. Cafferty, G. Tomlinson, Characterization of automotive dampers using higher order frequency response functions, Proc. Inst. Mech. Eng. Part D: J. Automobile Eng. 211 (3) (1997) 181–203, https://doi.org/10.1243/0954407971526353.
[18] I. Tawfiq, T. Vinh, Contribution to the extension of modal analysis to non-linear structure using Volterra functional series, Mech. Syst. Signal Process. 17 (2) (2003) 379–407, https://doi.org/10.1006/mssp.2002.1499, URLhttp://www.sciencedirect.com/science/article/pii/S0888327002914998.
[19] A. Chatterjee, N.S. Vyas, Non-linear parameter estimation with Volterra series using the method of recursive iteration through harmonic probing, J. Sound Vib. 268 (4) (2003) 657–678, https://doi.org/10.1016/S0022-460X(02)01537-7, URLhttp://www.sciencedirect.com/science/article/pii/S0022460X02015377.

[20] A. Chatterjee, N.S. Vyas, Non-linear parameter estimation in multi-degree-of-freedom systems using multi-input Volterra series, Mech. Syst. Signal Process. 18 (3) (2004) 457–489, https://doi.org/10.1016/S0888-3270(03)00016-5, URLhttp://www.sciencedirect.com/science/article/pii/S0888327003000165.

[21] A. Chatterjee, Identification and parameter estimation of a bilinear oscillator using Volterra series with harmonic probing, Int. J. Non-Linear Mech. 45 (1) (2010) 12–20, https://doi.org/10.1016/j.ijnonlinmec.2009.08.007, URLhttp://www.sciencedirect.com/science/article/pii/S0020746209001632.

[22] R. Lin, T. Ng, Higher-order FRFs and their applications to the identifications of continuous structural systems with discrete localized nonlinearities, Mech. Syst. Signal Process. 108 (2018) 326–346, https://doi.org/10.1016/j.ymssp.2018.02.033, URLhttp://www.sciencedirect.com/science/article/pii/S0888327018300980.

[23] O. Scussel, S. da Silva, The harmonic probing method for output-only nonlinear mechanical systems, J. Braz. Soc. Mech. Sci. Eng. 39 (9) (2017) 3329–3341, https://doi.org/10.1007/s40430-017-0723-y.

[24] A. Chatterjee, Structural damage assessment in a cantilever beam with a breathing crack using higher order frequency response functions, J. Sound Vib. 329 (16) (2010) 3325–3334, https://doi.org/10.1016/j.jsv.2010.02.026, URLhttp://www.sciencedirect.com/science/article/pii/S0022460X10001495.

[25] C. Cheng, Z. Peng, W. Zhang, G. Meng, Volterra-series-based nonlinear system modeling and its engineering applications: a state-of-the-art review, Mech. Syst. Signal Process. 87 (2017) 340–364, https://doi.org/10.1016/j.ymssp.2016.10.029, URLhttp://www.sciencedirect.com/science/article/pii/S0888327016304393.

[26] S. Boyd, L. Chua, Fading memory and the problem of approximating nonlinear operators with Volterra series, IEEE Trans. Circuits Syst. 32 (11) (1985) 1150–1161, https://doi.org/10.1109/TCS.1985.1085649.

[27] Q. Ran, M.L. Xiao, Y.X. Hu, Nonlinear vibration with Volterra series method used in civil engineering: the Bouc – Wen hysteresis model of generalized frequency response, in: Advances in Measurements and Information Technologies, Vol. 530 of Applied Mechanics and Materials, Trans Tech Publications, 2014, pp. 561–566, https://doi.org/10.4028/www.scientific.net/AMM.530-531.561.

[28] G. Manson, K. Worden, Higher-Order Frequency Response Functions for Hysteretic Systems, Springer International Publishing, Cham, 2016, https://doi.org/10.1007/978-3-319-29739-218, pp. 191–201.

[29] J. Noël, M. Schoukens, Hysteretic benchmark with a dynamic nonlinearity, in: Workshop on Nonlinear System Identification Benchmarks, Brussels, Belgium, 2016, pp. 7–14.

[30] A.F. Esfahani, P. Dreesen, K. Tiels, J.-P. Noël, J. Schoukens, Parameter reduction in nonlinear state-space identification of hysteresis, Mech. Syst. Signal Process. 104 (2018) 884–895, https://doi.org/10.1016/j.ymssp.2017.10.017, URLhttp://www.sciencedirect.com/science/article/pii/S0888327017305502.

[31] A. Bajrić, J. Høgsberg, Estimation of hysteretic damping of structures by stochastic subspace identification, Mech. Syst. Signal Process. 105 (2018) 36–50, https://doi.org/10.1016/j.ymssp.2017.11.042, URLhttp://www.sciencedirect.com/science/article/pii/S0888327017306246.

[32] M. Rebillat, M. Schoukens, Comparison of least squares and exponential sine sweep methods for parallel hammerstein models estimation, Mech. Syst. Signal Process. 104 (2018) 851–865, https://doi.org/10.1016/j.ymssp.2017.11.015, URLhttp://www.sciencedirect.com/science/article/pii/S0888327017305976.

[33] K. Worden, R. Barthorpe, E. Cross, N. Dervilis, G. Holmes, G. Manson, T. Rogers, On evolutionary system identification with applications to nonlinear benchmarks, Mech. Syst. Signal Process. 112 (2018) 194–232, https://doi.org/10.1016/j.ymssp.2018.04.001, URLhttp://www.sciencedirect.com/science/article/pii/S0888327018301912.

[34] S. Guo, S. Yang, C. Pan, Dynamic modeling of magnetorheological damper behaviors, J. Intell. Mater. Syst. Struct. 17 (1) (2006) 3–14, https://doi.org/10.1177/1045389X06055860, arXiv: https://doi.org/10.1177/1045389X06055860.

[35] F. Giri, Y. Rochdi, A. Radouane, A. Brouri, F. Chaoui, Frequency identification of nonparametric Wiener systems containing backlash nonlinearities, Automatica 49 (1) (2013) 124–137, https://doi.org/10.1016/j.automatica.2012.08.043, URLhttp://www.sciencedirect.com/science/article/pii/S0005109812004864.

[36] M.F.M. Naser, F. Ikhouane, Hysteresis loop of the LuGre model, Automatica 59 (2015) 48–53, https://doi.org/10.1016/j.automatica.2015.06.006, URLhttp://www.sciencedirect.com/science/article/pii/S0005109815002344.

[37] X.-R. Huang, L. Jézéquel, S. Besset, L. Li, O. Sauvage, Nonlinear modal synthesis for analyzing structures with a frictional interface using a generalized Masing model, J. Sound Vib. 434 (2018) 166–191, https://doi.org/10.1016/j.jsv.2018.07.027, URLhttp://www.sciencedirect.com/science/article/pii/S0022460X18304711.

[38] F. Giri, A. Radouane, A. Brouri, F.-Z. Chaoui, Combined frequency-prediction error identification approach for Wiener systems with backlash and backlash-inverse operators, Automatica 50 (3) (2014) 768–783, https://doi.org/10.1016/j.automatica.2013.12.030, URLhttp://www.sciencedirect.com/science/article/pii/S000510981300589X.

[39] A. Radouane, F. Giri, F. Ikhouane, T. Ahmed-Ali, F.-Z. Chaoui, A. Brouri, System identification of a class of Wiener systems with hysteretic nonlinearities, Int. J. Adapt. Control Signal Process. 31 (3) (2017) 332–359, https://doi.org/10.1002/acs.2700, acs.2700.

[40] S.A.M. Martins, L.A. Aguirre, Sufficient conditions for rate-independent hysteresis in autoregressive identified models, Mech. Syst. Signal Process. 75 (2016) 607–617, https://doi.org/10.1016/j.ymssp.2015.12.031, URLhttp://www.sciencedirect.com/science/article/pii/S0888327015005968.

[41] H. Jeffreys, B. Jeffreys, Methods of Mathematical Physics, Cambridge University Press, 1999.

[42] R. Bouc, Forced vibration of mechanical systems with hysteresis, in: Proceedings of the fourth conference on non-linear oscillation Prague, Czechoslovakia, 1967.

[43] G.O. Maldonado, Stochastic response of single degree of freedom hysteretic oscillators, Faculty of Virginia Polytechnic Institute and State University, 1987 (Master's thesis).

[44] C. Wong, Y.Q. Ni, J.M. Ko, Steady-state oscillation of hysteretic differential model. II: Performance analysis, J. Eng. Mech. 120 (11) (1994) 2299–2325, https://doi.org/10.1061/(ASCE)0733-9399(1994)120:11(2299).

[45] F. Ikhouane, J.E. Hurtado, J. Rodellar, Variation of the hysteresis loop with the Bouc-Wen model parameters, Nonlinear Dyn. 48 (4) (2007) 361–380, https://doi.org/10.1007/s11071-006-9091-3.

[46] T.T. Baber, Y.-K. Wen, Random vibration hysteretic, degrading systems, J. Eng. Mech. Div. 107 (6) (1981) 1069–1087.

[47] M. Schetzen, The Volterra and Wiener Theories of Nonlinear Systems, John Wiley and Sons, 1980.

[48] G. Tomlinson, G. Manson, G. Lee, A simple criterion for establishing an upper limit to the harmonic excitation level of the Duffing oscillator using the Volterra series, J. Sound Vib. 190 (5) (1996) 751–762, https://doi.org/10.1006/jsvi.1996.0091, URLhttp://www.sciencedirect.com/science/article/pii/S0022460X96900917.

[49] X.J. Jing, Z.Q. Lang, S.A. Billings, Frequency domain analysis for nonlinear volterra systems with a general non-linear output function, Int. J. Control 81 (2) (2008) 235–251, https://doi.org/10.1080/00207170701516389, arXiv: https://doi.org/10.1080/00207170701516389.

[50] K. Worden, G. Manson, G. Tomlinson, A hamonic probing algorithm for the multi-input Volterra series, J. Sound Vib. 201 (1) (1997) 67–84, https://doi.org/10.1006/jsvi.1996.0746, URLhttp://www.sciencedirect.com/science/article/pii/S0022460X96907464.

[51] A.K. Swain, S.A. Billings, Generalized frequency response function matrix for mimo non-linear systems, Int. J. Control 74 (8) (2001) 829–844, https://doi.org/10.1080/00207170010030144, arXiv: https://doi.org/10.1080/00207170010030144.

[52] S.B. Shiki, S. da Silva, M.D. Todd, On the application of discrete-time Volterra series for the damage detection problem in initially nonlinear systems, Struct. Health Monit. 16 (1) (2017) 62–78, https://doi.org/10.1177/1475921716662142, arXiv: http://shm.sagepub.com/content/early/2016/08/24/1475921716662142.full.pdf+html.

[53] J. Noël, A. Esfahani, G. Kerschen, J. Schoukens, A nonlinear state-space approach to hysteresis identification, Mech. Syst. Signal Process. 84 (Part B) (2017) 171–184, https://doi.org/10.1016/j.ymssp.2016.08.025, recent advances in nonlinear system identification.http://www.sciencedirect.com/science/article/pii/S0888327016303089.

[54] I. Kovacic, M.J. Brennan, The Duffing Equation: Nonlinear Oscillators and Their Behaviour, John Wiley & Sons, 2011.